

# Fast and robust animal pose estimation

Jacob M. Graving<sup>1,2,3,\*</sup>, Daniel Chae<sup>4</sup>, Hemal Naik<sup>1,2,3,5</sup>, Liang Li<sup>1,2,3</sup>, Benjamin Koger<sup>1,2,3</sup>, Blair R. Costelloe<sup>1,2,3</sup>, Iain D. Couzin<sup>1,2,3,\*</sup>

\*For correspondence:

jgraving@gmail.com;  
icouzin@orn.mpg.de

<sup>1</sup>Department of Collective Behaviour, Max Planck Institute for Ornithology, 78464 Konstanz, Germany; <sup>2</sup>Chair of Biodiversity and Collective Behaviour, University of Konstanz, 78464 Konstanz, Germany; <sup>3</sup>Centre for the Advanced Study of Collective Behaviour, University of Konstanz, 78464 Konstanz, Germany; <sup>4</sup>Department of Computer Science, Princeton University, 08544 Princeton, NJ, USA; <sup>5</sup>Chair for Computer Aided Medical Procedures, Technische Universität München, 80333 Munich, Germany

**Abstract** Quantitative behavioral measurements are important for answering questions across scientific disciplines—from neuroscience to ecology. State-of-the-art deep-learning methods offer major advances in data quality and detail by allowing researchers to automatically estimate locations of an animal's body parts directly from images or videos. However, currently-available animal pose estimation methods have limitations in speed and robustness. Here we introduce an easy-to-use open-source software toolkit, *DeepPoseKit*, that addresses these problems. Using modern desktop hardware, our methods perform real-time measurements at ~30–110-Hz with offline performance >1000-Hz—approximately 2× faster than current methods. We also achieve these results without significantly increasing measurement error compared to the most-accurate methods currently available. We demonstrate the versatility of our approach with multiple challenging animal pose estimation tasks in laboratory and field settings—including groups of interacting individuals. Our work reduces barriers to using advanced tools for measuring behavior and has broad applicability across the behavioral sciences.

## Introduction

Understanding the relationships between individual behavior, brain activity (reviewed by *Krakauer et al. 2017*), and collective and social behaviors (*Rosenthal et al., 2015; Strandburg-Peshkin et al., 2013; Jolles et al., 2017; Klibaite et al., 2017; Klibaite and Shaevitz, 2019*) is a central goal of the behavioral sciences—a field that spans disciplines from neuroscience to psychology, ecology, and genetics. Measuring and modelling behavior is key to understanding these multiple scales of complexity, and, with this goal in mind, researchers in the behavioral sciences have begun to integrate theory and methods from physics, computer science, and mathematics (*Anderson and Perona, 2014; Berman, 2018; Brown and De Bivort, 2018*). A cornerstone of this interdisciplinary revolution is the use of state-of-the-art computational tools, such as computer vision algorithms, to automatically measure locomotion and body posture (*Dell et al., 2014*). Such a rich description of animal movement then allows for modeling, from first principles, the full behavioral repertoire of animals (*Berman et al., 2014a, 2016; Wiltchko et al., 2015; Johnson et al., 2016; Todd et al., 2017; Klibaite et al., 2017; Markowitz et al., 2018; Klibaite and Shaevitz, 2019; Costa et al., 2019*). Tools for automatically measuring animal movement represent a vital first step toward developing unified theories of behavior across scales (*Berman, 2018; Brown and De Bivort, 2018*). Therefore,

technical factors like scalability, robustness, and usability are issues of critical importance, especially as researchers across disciplines begin to increasingly rely on these methods.

Two of the most recent contributions to the growing toolbox for quantitative behavioral analysis are from *Mathis et al. (2018)* and *Pereira et al. (2019)*, who make use of a popular type of machine learning model called *convolutional neural networks*, or *CNNs* (*LeCun et al. 2015*; Appendix 1), to automatically measure detailed representations of animal posture—structural *keypoints*, or *joints*, on the animal's body—directly from images and without markers. While these methods offer a major advance over conventional methods with regard to data quality and detail, they have disadvantages in terms of speed and robustness, which may limit their practical applications. To address these problems, we introduce a new software toolkit called *DeepPoseKit* that is fast, robust, and easy-to-use. We run experiments using multiple datasets to compare our new methods with the underlying pose estimation models from *Mathis et al. (2018)* and *Pereira et al. (2019)*. We find that our approach offers considerable improvements over currently-available methods. These results also demonstrate the flexibility of our toolkit for both laboratory and field situations and exemplify that our work is widely applicable across a range of species and experimental conditions.

## Animal pose estimation using deep learning

In the past, conventional methods for measuring posture with computer vision relied on species-specific algorithms (*Uhlmann et al., 2017*), highly-specialized or restrictive experimental setups (*Mendes et al., 2013*; *Kain et al., 2013*), attaching intrusive physical markers to the study animal (*Kain et al., 2013*), or some combination thereof. These methods also typically required expert computer-vision knowledge to use, were limited in the number or type of body parts that could be tracked (*Mendes et al., 2013*), involved capturing and handling the study animals to attach markers (*Kain et al., 2013*)—which is not possible for many species—and despite best efforts to minimize human involvement, often required manual intervention to correct errors (*Uhlmann et al., 2017*). All of these methods were built to work for a small range of conditions and typically required considerable effort to adapt to novel contexts.

In contrast to conventional computer-vision methods, modern deep-learning-based methods can be used to achieve human-level accuracy in nearly any context by manually annotating data (Figure 1)—known as a *training set*—and training a general-purpose image-processing algorithm—a convolutional neural network or CNN—to automatically estimate the locations of an animal's body parts directly from images (Figure 2). State-of-the-art machine learning methods, like CNNs, use these training data to parameterize a model of the relationship between a set of input data—i.e. images—and the desired output distribution—i.e. posture keypoints. After adequate training, a model can be used to make predictions on previously-unseen data from the same dataset—inputs that were not part of the training set—which is known as *inference*. In other words, these models are able to generalize human-level expertise at scale after having been trained on only a relatively small number of examples. We provide more detailed background information on using CNNs for pose estimation in Appendices 1–6.

Similar to conventional pose estimation methods, the task of implementing deep-learning models in software and training them on new data is complex and requires expert knowledge. However, in most cases, once the underlying model and training routine are implemented, a high-accuracy pose estimation model for a novel context can be built with minimal modification—often just by changing the training data. With a simplified toolkit and high-level software interface designed by an expert, even scientists with limited computer-vision knowledge can begin to apply these methods to their research. Once the barriers for implementing and training a model are sufficiently reduced, the main bottleneck for using these methods becomes collecting an adequate training set—a labor-intensive task made less time-consuming by techniques described in Appendix 2.

*Mathis et al. (2018)* and *Pereira et al. (2019)* were the first to popularize the use of CNNs for animal pose estimation. These researchers built on work from the human pose estimation

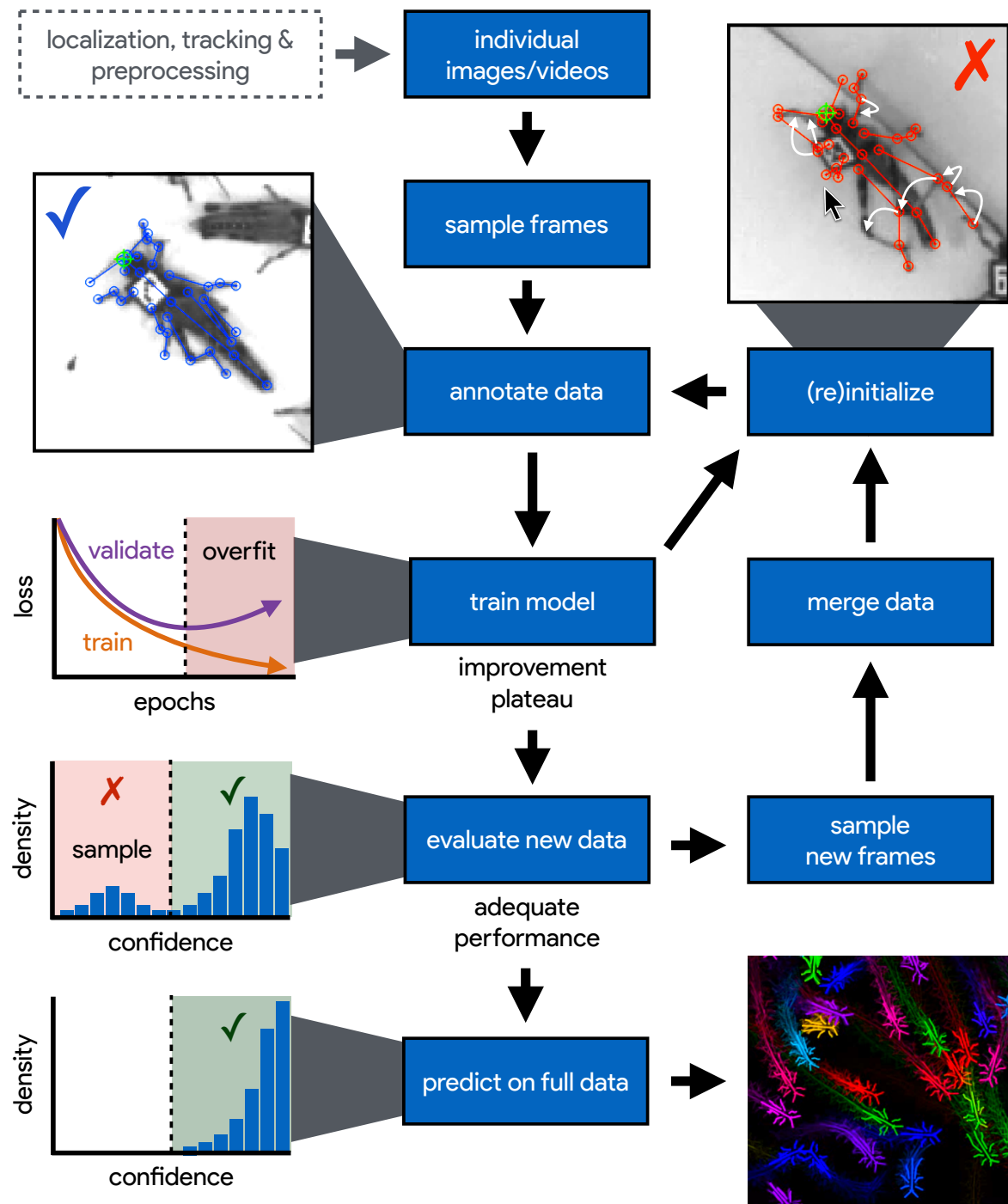


**Figure 1.** An illustration of the workflow for DeepPoseKit. Multi-individual images are localized, tracked, and preprocessed into individual images, which is not required for single-individual image datasets. An initial image set is sampled, annotated, and then iteratively updated using the active learning approach described by *Pereira et al. (2019)* (see Appendix 2). As annotations are made, the model is trained (Figure 2) with the current training set and keypoint locations are initialized for unannotated data to reduce the difficulty of further annotations. This is repeated until there is a noticeable improvement plateau in the initialized data and the annotator is providing only minor corrections. New data from the full dataset are evaluated with the model, and the training set is merged with new examples that are sampled based on the current model performance—shown here as the distribution of confidence scores from the confidence maps predicted by the model. This process is repeated as necessary until performance is adequate when evaluating new data. The pose estimation model can then be used to make predictions for the full data set, which can then be used for further analysis.

**Figure 1-video 1.** A visualization of the posture data output for a group of locusts (5x speed).

literature (e.g. *Andriluka et al. 2014*; *Insafutdinov et al. 2016*; *Newell et al. 2016*) using a type of fully-convolutional neural network or F-CNN (*Long et al. 2015*; Appendix 3) often referred to as an encoder-decoder model (Appendix 3 Box 1). These models are used to measure animal posture by training the network to transform images into probabilistic estimates of keypoint locations, known as *confidence maps* (shown in Figure 2), that describe the body posture for one or more individuals. These confidence maps are processed to produce the 2-D spatial coordinates of each keypoint, which can then be used for further analysis. The methods from *Mathis et al. (2018)* can be used to estimate posture for single individuals—known as *individual pose estimation*—or multiple individuals simultaneously—known as *multiple pose estimation*. In contrast, the methods from *Pereira et al. (2019)* are limited to individual pose estimation. The methods we present in this paper are technically limited to individual pose estimation; however, we successfully remove this limitation and extend our methods to groups of interacting individuals by first localizing and tracking individuals using additional software (see Appendix 4 for discussion).

*Mathis et al. (2018)* developed their software toolkit—DeepLabCut—by modifying a previously-published pose estimation model called *DeeperCut* (*Insafutdinov et al., 2016*), which is built on the popular *ResNet* architecture (*He et al., 2016*)—a state-of-the-art model for image classification. This choice is advantageous because the use of a popular architecture allows for incorporating a pre-trained encoder to improve performance and reduce the number of required training examples (*Mathis et al., 2018*), known as *transfer learning* (*Pratt 1993*; Appendix 2). However, this choice is also disadvantageous as the model is *overparameterized* with >25 million parameters. Overparameterization allows the model to make accurate predictions, but this may come with the cost of slow inference. Work from *Mathis and Warren (2018)* showed the inference speed for DeepLabCut (*Mathis et al., 2018*) can be improved by decreasing the resolution of input images, but this is achieved at the expense of accuracy. Recent updates to the DeepLabCut toolkit include considerable efforts to improve performance and ease-of-use by organizing the code into a Python package that includes a custom annotation tool and updated training routine—amongst other improvements (see *Nath et al. 2018*).

With regard to model design, *Pereira et al. (2019)* implement a modified version of a model called *SegNet* (*Badrinarayanan et al., 2015*), which they call *LEAP* (LEAP Estimates Animal Pose), that attempts to limit model complexity and overparameterization with the goal of maximizing inference speed (see Appendix 6)—although the results from our comparisons suggest this strategy achieved only limited success compared to DeepLabCut (*Mathis et al., 2018*). LEAP is advantageous because it is explicitly designed for fast inference but has disadvantages such as a lack of robustness to data variance, like rotations or shifts in lighting, and an inability to generalize to new experimental setups. Additionally, to achieve maximum performance, the LEAP framework requires computationally expensive preprocessing that is not practical for many datasets, which makes it unsuitable for a wide range of experiments (see Appendix 6 for more details). The software from *Pereira et al. (2019)* is feature-rich (see Appendix 2) and generally easy to install and use. However, much of the interface is written in MATLAB (The Mathworks Inc.), which requires an expensive and restrictive software license.

Together the methods from *Mathis et al. (2018)* and *Pereira et al. (2019)* represent the two extremes of a phenomenon known as the *speed-accuracy trade-off* (*Huang et al., 2017b*)—an active area of research in the machine learning literature. *Mathis et al. (2018)* prioritize accuracy over speed by using a large overparameterized model (*Insafutdinov et al., 2016*), and *Pereira et al. (2019)* prioritize speed over accuracy by using a smaller less-robust model. While this speed-accuracy trade-off can limit the capabilities of CNNs, there has been extensive work to make these models more efficient without impacting accuracy (e.g. *Chollet 2017*; *Huang et al. 2017a*; *Sandler et al. 2018*). To address the limitations of this trade-off, we apply recent developments from the machine learning literature and provide an effective solution to the problem. In the case of F-CNN models used for pose estimation, improvements in efficiency and robustness have been made through the use of *multi-scale inference* (Appendix 3 Box 1) and by increasing the number of connections



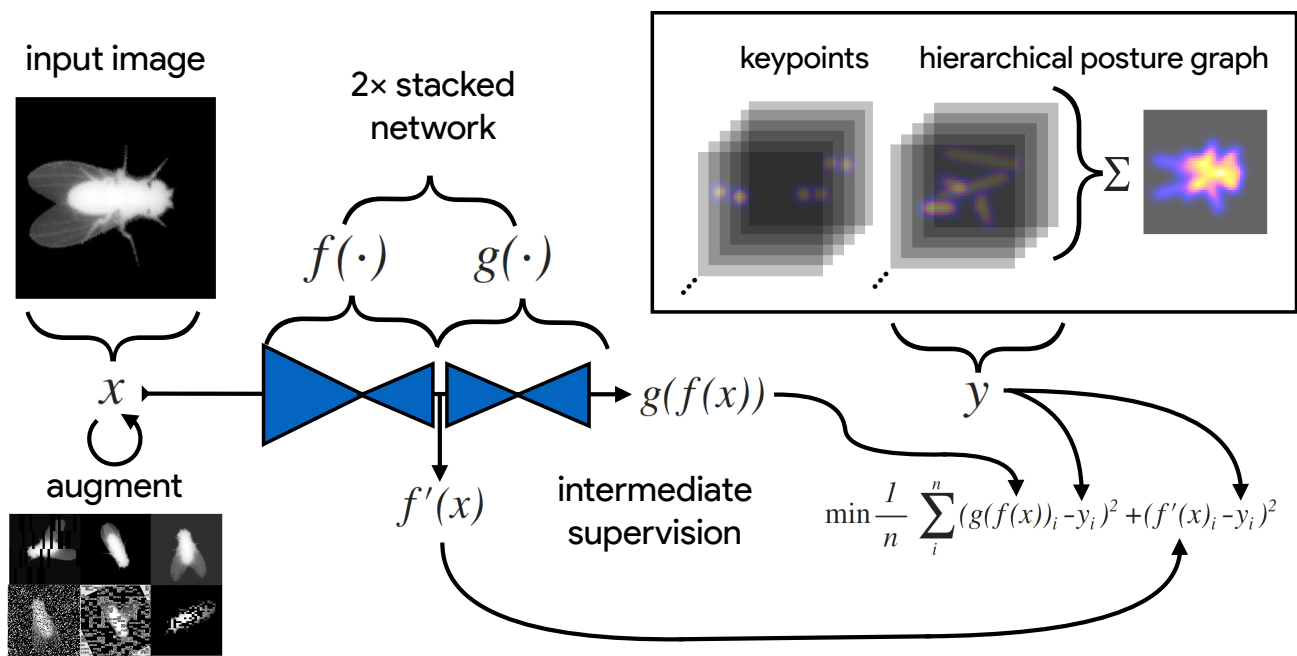


**Figure 2.** An illustration of the model training process for DeepPoseKit (see Appendix 1 for details about training models). Input images  $x$  (**top-left**) are augmented (**bottom-left**) with various spatial transformations (rotation, translation, scale, etc.) followed by noise transformations (dropout, additive noise, blurring, contrast, etc.) to improve the robustness and generalization of the model. The ground truth annotations are then transformed with matching spatial augmentations (not shown for the sake of clarity) and used to draw the confidence maps  $y$  for the keypoints and hierarchical posture graph (**top-right**). The images  $x$  are then passed through the network to produce a multidimensional array  $g(f(x))$ —a stack of images corresponding to the keypoint and posture graph confidence maps for the ground truth  $y$ . Mean squared error between the outputs for both hourglass networks  $g(f(x))$  and  $f'(x)$  and the ground truth data  $y$  is then minimized (**bottom-right**), where  $f'(x)$  indicates a subset of the output from  $f(x)$ —only those feature maps being optimized to reproduce the confidence maps for the purpose of intermediate supervision (Appendix 5). The loss function is minimized until the validation loss stops improving—indicating that the model has converged or is starting to overfit to the training data.

143 between layers in the model (Appendix 3 Figure 1)—both of which we incorporate into our methods.

## 144 Methods and Results

145 Here we introduce fast, flexible, and robust pose estimation methods with a software interface  
 146 that emphasizes usability. Our methods build on the state-of-the-art for individual pose estimation  
 147 (Newell et al. 2016; Appendix 5), convolutional regression models (Jégou et al. 2017; Appendix  
 148 3 Box 1), and conventional computer vision algorithms (Guizar-Sicairos et al., 2008) to improve  
 149 model efficiency and achieve faster, more accurate results on multiple challenging pose estimation  
 150 tasks. We developed two model implementations—including a new model architecture that we call  
 151 *Stacked DenseNet*—and a new method for processing confidence maps called *subpixel maxima* that  
 152 provides fast and accurate results with subpixel precision—even at low resolutions. We also discuss  
 153 a modification to incorporate the global geometry between keypoints when training pose estimation  
 154 models that increases accuracy without decreasing speed. We ran experiments to optimize our  
 155 approach and compared our models to those from Mathis et al. (2018) (DeepLabCut) and Pereira  
 156 et al. (2019) (LEAP) using three image datasets filmed in the laboratory and the field—including  
 157 multiple interacting individuals that were first localized and cropped from larger, multi-individual  
 158 images. While we apply localization to our datasets, this is not a requirement as long as the images  
 159 only contain single individuals.

## An end-to-end pose estimation framework

We provide a full-featured, extensible, and easy-to-use software package that is written entirely in the Python programming language (Python Software Foundation) and is built on the popular Keras deep-learning package (Chollet et al., 2015)—using TensorFlow as a backend (Abadi et al., 2015). Our software is a complete, end-to-end pipeline (Figure 1) with a custom GUI (graphical user interface) for creating annotated training data with *active learning* similar to Pereira et al. (2019; Appendix 2), as well as an interface for *data augmentation* (Jung 2018; Appendix 2; shown in Figure 2), model training and evaluation (Figure 2; Appendix 1), and running inference on new data. We designed our high-level programming interface to be a testbed for experimentation, allowing the user to go from idea to execution as quickly as possible, and we organized our software into a Python module called *DeepPoseKit*. The code, documentation, and examples for our entire software package are freely available at <https://github.com/jgraving/deepposekit> under a permissive open-source license.

## Our pose estimation models

To achieve the goal of “fast animal pose estimation” introduced by Pereira et al. (2019), while also wanting to achieve the robust predictive power of models like DeepLabCut (Mathis et al., 2018), we implemented two fast pose estimation models that extend the current state-of-the-art for individual pose estimation introduced by Newell et al. (2016) and the current state-of-the-art for convolutional regression from Jégou et al. (2017). Our model implementations use fewer parameters than both DeepLabCut (Mathis et al., 2018) and LEAP (Pereira et al., 2019) while simultaneously removing many of the limitations of these architectures.

In order to limit overparameterization while minimizing performance loss, we designed our models to allow for multi-scale inference (Appendix 3 Box 1) while optimizing our model hyperparameters for efficiency. Our first model is a novel implementation of *FC-DenseNet* from Jégou et al. (2017; Appendix 3 Box 1) arranged in a stacked configuration similar to Newell et al. (2016; Appendix 5). We call this new model *Stacked DenseNet*, and to the best of our knowledge, this is the first implementation of this architecture in the literature—for pose estimation or otherwise. Further details for this model are available in Appendix 8. Our second model is a modified version of the *Stacked Hourglass* model from Newell et al. (2016; Appendix 5) with hyperparameters that allow for changing the number of filters in each convolutional block to constrain the number of parameters—rather than using 256 filters for all layers as described in Newell et al. (2016).

## Subpixel keypoint prediction on the GPU

In addition to implementing our efficient pose estimation models, we developed a new method to process the model outputs to allow for faster, more accurate predictions. When using a fully-convolutional posture estimation model, the confidence maps produced by the model must be converted into coordinate values for the predictions to be useful, and there are typically two choices for making this conversion. The first is to move the confidence maps out of GPU memory and post-process them on the CPU. This solution allows for easy, flexible, and accurate calculation of the coordinates with subpixel precision (Insafutdinov et al., 2016; Mathis et al., 2018). However, CPU processing is not ideal because moving large arrays of data between the GPU and CPU can be costly, and computation on the CPU is generally slower. The other option is to directly process the confidence maps on the GPU and then move the coordinate values from the GPU to the CPU. This approach usually means converting confidence maps to integer coordinates based on the row and column index of the global maximum for each confidence map (Pereira et al., 2019). However, this means that, to achieve a precise estimation, the confidence maps should be predicted at the full resolution of the input image, or larger, which slows down inference speed.

As an alternative to these two strategies, we introduce a new GPU-based convolutional layer that we call *subpixel maxima*. This layer uses the fast, efficient, image registration algorithm introduced by Guizar-Sicairos et al. (2008) to translationally align a centered two-dimensional Gaussian filter

to each confidence map via Fourier-based convolution. The translational shift between the filter and each confidence map allows us to calculate the coordinates of the global maxima with high speed and subpixel precision. This technique allows for accurate predictions even if the model's confidence maps are dramatically smaller than the resolution of the input image.

## Learning global relationships between keypoints

Minimizing extreme prediction errors is important to prevent downstream effects on any further behavioral analysis—especially in the case of analyses based on time-frequency transforms like those from *Berman et al. (2014a, 2016)*; *Klibaite et al. (2017)*; *Todd et al. (2017)*; *Klibaite and Shae-vitz (2019)* and *Pereira et al. (2019)* where high magnitude errors can cause inaccurate behavioral classifications. One way to minimize extreme errors when estimating posture is to incorporate multiple spatial scales when making predictions. Our pose estimation models are *implicitly* capable of using information from multiple spatial scales (see Appendix 3 Box 1), but there is no *explicit* signal that optimizes the model to take advantage of this information when making predictions.

To remedy this, we modified the model's output to predict, in addition to the keypoint locations, a hierarchical graph of edges describing the global geometry between keypoints—similar to the part affinity fields described by *Cao et al. (2017)*. This was achieved by adding an extra set of confidence maps to the output where edges in the postural graph are represented by Gaussian-blurred lines the same width as the Gaussian peaks in the keypoint confidence maps. Our posture graph output then consists of four levels: (1) a set of confidence maps for the smallest limb segments in the graph (e.g. foot to ankle, knee to hip, etc.; Figure 2), (2) a set of confidence maps for individual limbs (e.g. left leg, right arm, etc.; Figure 3), (3) a map with the entire postural graph, and (4) a fully-integrated map that incorporates the entire posture graph and confidence peaks for all of the joint locations (Figure 2). Each level of the hierarchical graph is built from lower levels in the output, which forces the model to learn correlated features across multiple scales when making predictions.

## Experiments and model comparisons

We ran three experiments to test and optimize our approach. First, we compared our new subpixel maxima layer to an integer-based global maxima with downsampled outputs ranging from  $1\times$  to  $\frac{1}{16}\times$  the input resolution using our Stacked DenseNet model. Next, we tested if training a Stacked DenseNet model to predict the global geometry of the posture graph improves accuracy. Finally, we compared our model implementations of Stacked Hourglass and Stacked DenseNet to the models from *Pereira et al. (2019)* (LEAP) and *Mathis et al. (2018)* (DeepLabCut), which we also implemented in our framework (see Appendix 8 for details on our implementation of *Mathis et al. (2018)*). While we do compare our models to DeepLabCut (*Mathis et al., 2018*) we do not use the same training routine as *Mathis et al. (2018)* and *Nath et al. (2018)*. This distinction makes direct comparisons between our frameworks—DeepPoseKit and DeepLabCut—difficult, and testing multiple training routines would make our comparisons prohibitively complex. However, because the prediction task is functionally identical—i.e. predicting confidence maps from images—and we apply data augmentations similar to those introduced by *Nath et al. (2018)*, any differences between training routines should have minimal effect on performance. When benchmarking these models we incorporated the relevant improvements from our experiments—including subpixel maxima and predicting global geometry between keypoints—unless otherwise noted (see Appendix 8).

## Datasets

We performed experiments using the vinegar or "fruit" fly (*Drosophila melanogaster*) dataset (Figure 3-video 1) provided by *Pereira et al. (2019)*, and to demonstrate the versatility of our methods we also compared model performance across two previously unpublished posture data sets from groups of desert locusts (*Schistocerca gregaria*) filmed in a laboratory setting (Figure 3-video 2), and herds of Grévy's zebras (*Equus grevyi*) filmed in the wild (Figure 3-video 3). Our locust dataset was filmed from above using a high-resolution camera (Basler ace acA2040-90umNIR) and video

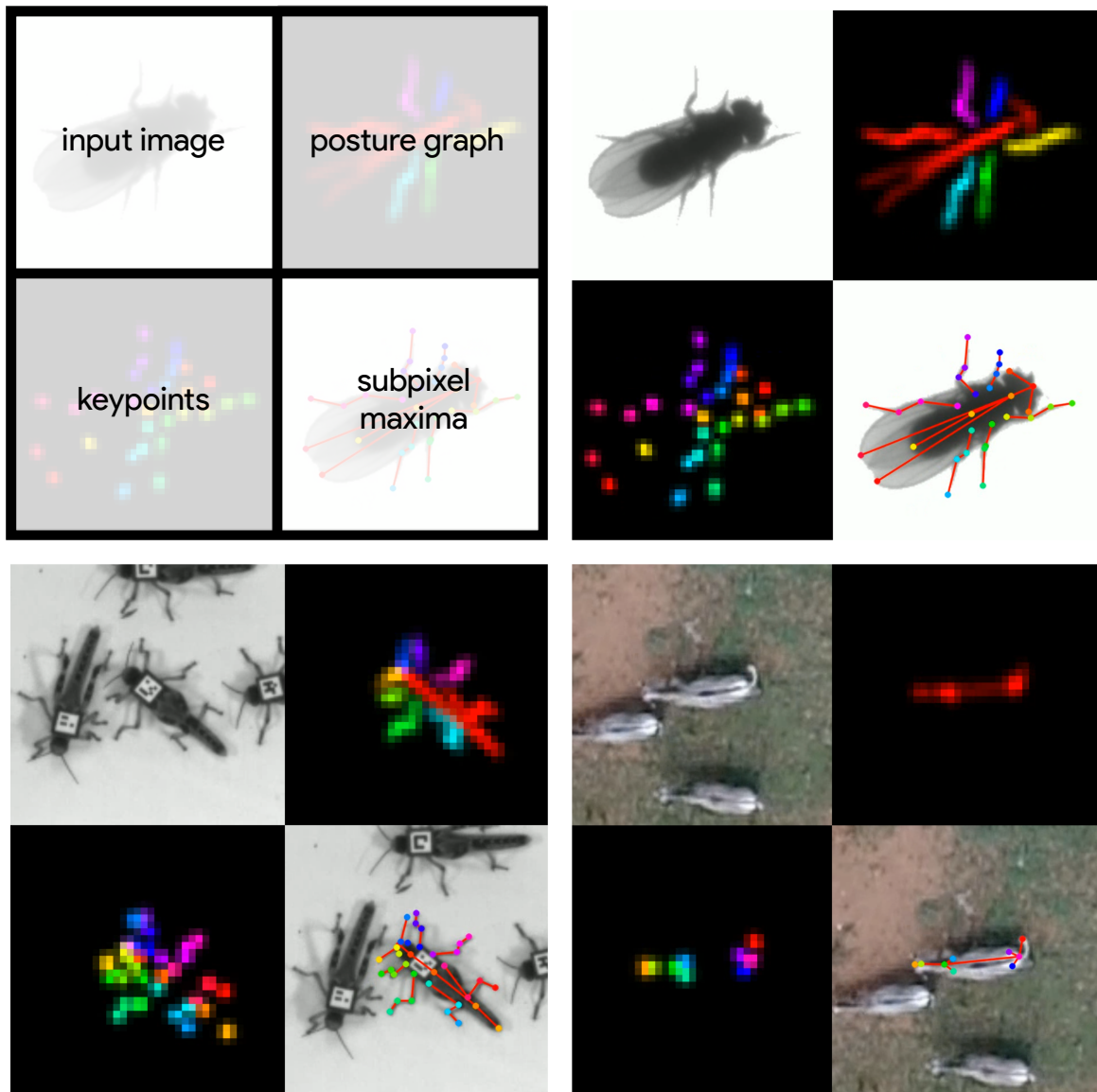


**Figure 3.** A visualization of the datasets we used to evaluate our methods (Table 1). For each dataset, confidence maps for the keypoints (bottom-left) and posture graph (top-right) are illustrated using different colors for each map. These outputs are from our Stacked DenseNet model at  $\frac{1}{4}\times$  resolution.

**Figure 3-video 1.** A video of a behaving fly from *Pereira et al. (2019)* with pose estimation outputs visualized.

**Figure 3-video 2.** A video of a behaving locust with pose estimation outputs visualized.

**Figure 3-video 3.** A video of a behaving Grévy's zebra with pose estimation outputs visualized.

**Table 1.** Datasets used for model comparisons.

Name	Species	Resolution	# Images	# Keypoints	Individuals	Source
Vinegar fly	<i>Drosophila melanogaster</i>	192×192	1500	32	Single	<i>Pereira et al. (2019)</i>
Desert locust	<i>Schistocerca gregaria</i>	160×160	800	35	Multiple	This paper
Grévy's zebra	<i>Equus grevyi</i>	160×160	1000	9	Multiple	This paper

recording system (Motif, loopbio GmbH), and our zebra dataset was filmed from above using a commercially-available quadcopter drone (DJI Phantom 4 Pro). Individuals in the videos were positionally tracked and the videos were then cropped using the egocentric coordinates of each individual and saved as separate videos—one for each individual. Further details of how these image datasets were acquired, preprocessed, and tracked before applying our pose estimation methods will be described elsewhere. The locust and zebra datasets are particularly challenging as they feature multiple interacting individuals—with focal individuals centered in the frame—and the latter with highly-variable light conditions. Before training each model we split each data set into randomly selected training and validation sets with 90% training examples and 10% validation examples. The details for each dataset are described in Table 1.

### Model training

For each experiment, we set our model hyperparameters to the same configuration and all models were trained with  $\frac{1}{4} \times$  resolution outputs and a stack of two hourglasses with two outputs where loss was applied (see Figure 2). Although our model hyperparameters could be infinitely adjusted to trade off between speed and accuracy, we compared only one configuration for each of our model implementations. These results are not meant to be an exhaustive search of model configurations as the best configuration will depend on the application. The details of the hyperparameters we used for each model are described in Appendix 8.

To make our posture estimation tasks closer to realistic conditions and properly demonstrate the robustness of our methods to rotation, translation, and scale, we applied various augmentations to each data set during training. All models were trained using data augmentations that included random flipping, or mirroring, along both image axes with 0.5 probability, random rotations around the center of the image in the range  $[-180^\circ, +180^\circ]$ , random scaling between  $[90\%, 110\%]$  for flies and locusts, random scaling between  $[75\%, 125\%]$  for zebras to account for greater size variation in the data set, and random translations in the range  $[-5\%, +5\%]$ . After performing these spatial augmentations we also applied a variety of noise augmentations that included multiple types of additive noise, dropout, blurring, and contrast augmentations to further ensure robustness and generalization.

We trained our models (Figure 2) using mean squared error loss optimized using the ADAM optimizer (Kingma and Ba, 2014) with a learning rate of  $1 \times 10^{-3}$  and a batch size of 16. We lowered the learning rate by a factor of 5 each time the validation loss did not improve by more than  $1 \times 10^{-3}$  for 10 epochs. We considered models to be converged when the validation loss stopped improving for 50 epochs, and we calculated validation error as the Euclidean distance between predicted and ground-truth image coordinates for only the best performing version of the model, which we evaluated at the end of each epoch during optimization. We performed this procedure five times for each experiment and randomly selected a new validation set for each replicate.

### Model evaluation

Machine learning models are typically evaluated for their ability to generalize to new data, known as *predictive performance*, using a held-out *test set*—a subsample of annotated data that is not used for training or validation. However, when fitting and evaluating a model on a small dataset, using an adequately-sized validation and test set can lead to erroneous conclusions about the predictive



performance of the model if the training set is too small (*Kuhn and Johnson, 2013*). Therefore, to maximize the size of the training set, we elected to use only a validation set for model evaluation.

Generally a test set is used to avoid biased performance measures caused by overfitting the model hyperparameters to the validation set. However, we did not adjust our model architecture to achieve better performance on our validation set—only to achieve fast inference speeds. While we did use validation error to decide when to lower the learning rate during training and when to stop training, lowering the learning rate in this way should have no effect on the generalization ability of the model, and because we heavily augment our training set during optimization—forcing the model to learn a much larger image distribution than what is included in the training and validation sets—overfitting to the validation set is unlikely. We also demonstrate the generality of our results for each experiment by randomly selecting a new validation set with each replicate. All of these factors make the Euclidean error for the unaugmented validation set a reasonable measure of the predictive performance for each model.

The inference speed for each model was assessed by running predictions on 100,000 randomly generated images with a batch size of 1 for real-time speeds and a batch size of 100 for offline speeds. Our hardware consisted of a Dell Precision Tower 7910 workstation (Dell, Inc.) running Ubuntu Linux v18.04 with 2× Intel Xeon E5-2623 v3 CPUs (8 cores, 16 threads at 3.00GHz), 64GB of RAM, a Quadro P6000 GPU and a Titan Xp GPU (NVIDIA Corporation). We used both GPUs for training models and evaluating predictive performance, and we only used the faster Titan Xp GPU for benchmarking inference speeds. While the hardware we used for development and testing is quite advanced, there is no requirement for this level of performance, and our software can easily be run on lower-end hardware. We evaluated inference speeds on multiple consumer-grade desktop computers and found similar performance ( $\pm 10\%$ ) when using the same GPU.

### Assessing prediction accuracy with Bayesian inference

To more rigorously assess performance differences between models, we parameterized the Euclidean error distribution for each experiment by fitting a Bayesian linear model with a Gamma-distributed likelihood function. This model takes the form:

$$\begin{aligned} p(y|X, \theta_\mu, \theta_\phi) &\sim \text{Gamma}(\alpha, \beta) \\ \alpha &= \mu^2 \phi^{-1} \\ \beta &= \mu \phi^{-1} \\ \mu &= h(X\theta_\mu) \\ \phi &= h(X\theta_\phi) \end{aligned}$$

where  $X$  is the design matrix composed of binary indicator variables for each pose estimation model,  $\theta_\mu$  and  $\theta_\phi$  are vectors of intercepts,  $h(\cdot)$  is the softplus function (*Dugas et al., 2001*)—or  $h(x) = \log(1 + e^x)$ —used to enforce positivity of  $\mu$  and  $\phi$ , and  $y$  is the Euclidean error of the pose estimation model. Parameterizing our error distributions in this way allows us to calculate the posterior distributions for the mean  $E[y] = \alpha\beta^{-1} \equiv \mu$  and variance  $\text{Var}[y] = \alpha\beta^{-2} \equiv \phi$ . This parameterization then provides us with a statistically rigorous way to assess differences in model accuracy in terms of both central tendency and spread—accounting for both epistemic uncertainty (unknown unknowns, e.g. parameter uncertainty) and aleatoric uncertainty (known unknowns, e.g. data variance). Details of how we fitted these models can be found in Appendix 7.

### Subpixel prediction allows for fast and accurate inference

We compared the accuracy of our subpixel maxima layer to an integer-based maxima layer using the fly dataset. We found significant accuracy improvements across every downsampling configuration (Appendix Figure 5). Even with confidence maps at  $\frac{1}{8}\times$  the resolution of the original image, error

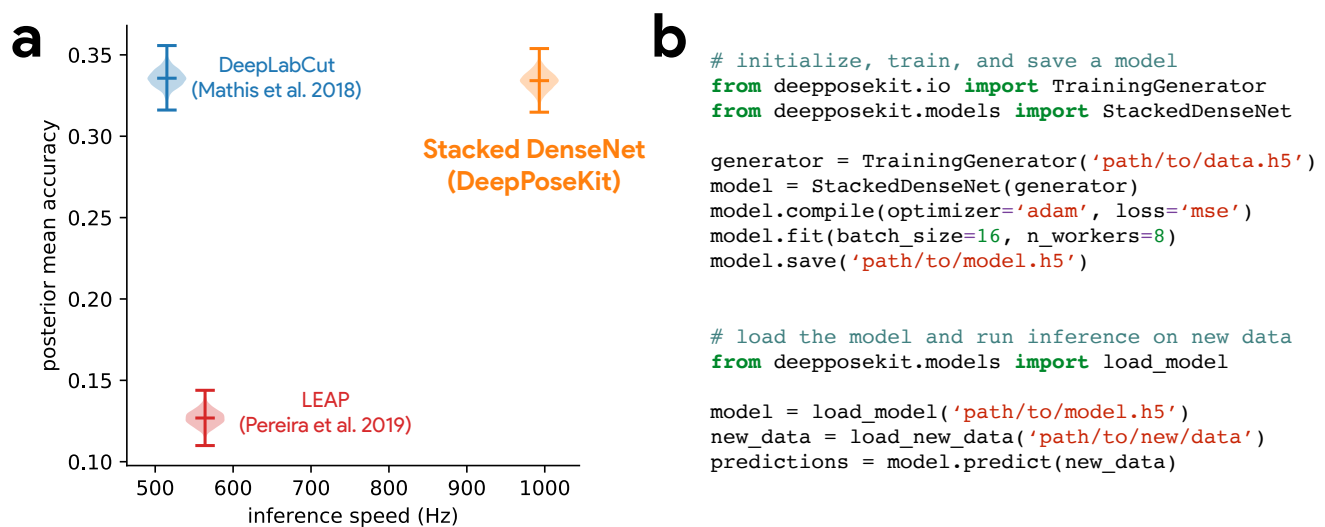


**Figure 4.** Our methods estimate posture at approximately 2x—or greater—the speed of LEAP (Pereira et al., 2019) and DeepLabCut (Mathis et al., 2018) while achieving similar accuracy to DeepLabCut (Mathis et al., 2018)—shown here as mean accuracy  $1/(1 + \text{Euclidean error})$  of our Stacked DenseNet model for our most challenging dataset of multiple interacting Grévy's zebras (*E. grevyi*) filmed in the wild (a). Our software interface is designed to be straightforward but flexible. We include many options for expert users to customize model training with sensible default settings to make pose estimation as easy as possible for beginners. For example, training a model and running inference on new data requires writing only a few lines of code and specifying some basic settings (b).

338 did not drastically increase compared to full-resolution predictions. Making predictions at such  
 339 a downsampled resolution allows us to achieve very fast inference >1000 Hz while maintaining  
 340 relatively high accuracy. Additionally, achieving fast pose estimation using CNNs typically relies on  
 341 massively parallel processing on the GPU with large batches of data or requires downsampling the  
 342 images to increase speed, which increases error (Mathis and Warren, 2018). These factors make  
 343 fast and accurate real-time inference challenging to accomplish. Our Stacked DenseNet model,  
 344 with a batch size of one, can run inference at ~30-110Hz—depending on resolution (Appendix  
 345 Figure 5a)—which could be further improved by downsampling the input image resolution or  
 346 reconfiguring the model with fewer parameters. This opens the door to real-time closed-loop  
 347 behavioral experiments with prediction errors similar to current state-of-the-art methods.

### 348 Predicting global geometry improves accuracy and reduces extreme errors

349 We find that forcing the pose estimation model to predict a hierarchical posture graph reduces  
 350 prediction error (Appendix Figure 6), and because the feature maps for the posture graph can be  
 351 removed from the final output during inference, this effectively improves prediction accuracy for  
 352 free. Both the mean and variance of the error distributions were lower when predicting the posture  
 353 graph, which suggests that learning global geometry both decreases error *on average* and helps to  
 354 reduce *extreme* prediction errors. The overall effect size for this decrease in error is fairly small (<1  
 355 pixel average reduction in error), but based on the results from the zebra dataset, this modification  
 356 more dramatically improves performance for datasets with higher-variance images and sparse  
 357 posture graphs. These results also suggest that annotating multiple keypoints to incorporate an  
 358 explicit signal for global information may help improve prediction accuracy for a specific body part  
 359 of interest.

### 360 Our models are fast and robust

361 Finally, we benchmarked our model implementations against the models from Pereira et al. (2019)  
 362 and Mathis et al. (2018). We find that our Stacked DenseNet model outperforms both LEAP (Pereira  
 363 et al., 2019) and DeepLabCut (Mathis et al., 2018) in terms of speed while also achieving much  
 364 higher accuracy than LEAP (Pereira et al., 2019) with similar accuracy to DeepLabCut (Mathis et al.,

2018) (Figure 4a). We found that both the Stacked Hourglass and Stacked DenseNet models outperformed LEAP (Pereira et al., 2019) with approximately 2x faster inference speeds and 3x higher mean accuracy. Not only were our models' average prediction error significantly improved, but also, importantly, the variance was lower—indicating that our models produced fewer extreme prediction errors. At  $\frac{1}{4}$ x resolution, our Stacked DenseNet implementation consistently achieved prediction accuracy nearly identical to Mathis et al. (2018) while running inference at nearly 2x the speed and using only ~2% of the parameters— ~26 million vs. ~0.5 million. The inference speed could be further improved by using a  $\frac{1}{8}$ x output without much increase in error (Appendix Figure 5) or by further adjusting the hyperparameters to constrain the size of the model. Our Stacked Hourglass implementation followed closely behind this level of performance but consistently performed worse than our Stacked DenseNet model. We were also able to reproduce the results reported by Pereira et al. (2019) that LEAP and the Stacked Hourglass model from Newell et al. (2016) have similar average prediction error for the fly dataset. However, we also find that LEAP (Pereira et al., 2019) has much higher variance, which suggests it is more prone to extreme prediction errors—a problem for further data analysis. Detailed results of our model comparisons are shown in Appendix Figure 7.

## Discussion

Here we have presented a new framework for estimating animal posture using deep learning models. We built on the state-of-the-art for individual pose estimation using convolutional neural networks to achieve fast inference without substantially reducing accuracy. Our pose estimation models offer considerable improvements (Figure 4a) over those from Mathis et al. (2018) (DeepLabCut) and Pereira et al. (2019) (LEAP) while also providing a simplified interface (Figure 4b) for using these advanced tools to measure animal behavior and locomotion. We tested our methods across a range of datasets from controlled laboratory environments with single individuals to challenging field situations with multiple interacting individuals and variable lighting conditions. We found that our methods perform well for all of these situations. We ran experiments to optimize our approach and discovered that some straightforward modifications can greatly improve speed and accuracy. Additionally, we demonstrated that these modifications improve not just the average error but also help to reduce extreme prediction errors—a key determinant for the reliability of subsequent statistical analysis.

While our results offer a good-faith comparison of the available methods for animal pose estimation, there is inherent uncertainty that we have attempted to account for but may still bias our conclusions. For example, deep learning models are trained using stochastic algorithms that give different results with each replicate, and the Bayesian statistical methods we use for comparison are explicitly probabilistic in nature. There is also great variability across hardware and software configurations when using these models in practice (Mathis and Warren, 2018), so performance may change across experimental setups. Additionally, we demonstrated that some models may perform better than others for specific applications (Appendix Figure 7), and to account for this, our toolkit offers researchers the ability to choose the model that best suits their requirements—including LEAP (Pereira et al., 2019) and DeepLabCut (Mathis et al., 2018).

We highlighted important considerations when using CNNs for pose estimation and reviewed the progress of fully-convolutional regression models from the literature. Recent advancements for these models have been driven mostly by a strategy of adding more connections between layers to increase performance and efficiency (e.g. Jégou et al. 2017). New fundamentally-different models (Sabour et al., 2017) and loss functions (Chen et al., 2017) may provide further performance improvements. Recent work (e.g. Weigert et al. 2018; Roy et al. 2018) has also shown that future progress may require more mathematically-principled approaches such as applying probabilistic concepts (Kendall and Gal, 2017) and Bayesian inference at scale (Tran et al., 2018).

Measuring behavior is an critical factor for many studies in neuroscience (Krakauer et al., 2017). Understanding the connections between brain activity and behavioral output requires

detailed and objective descriptions of body posture that match the richness and resolution neural measurement technologies have provided for years (*Anderson and Perona, 2014; Berman, 2018; Brown and De Bivort, 2018*), which our methods and other deep-learning-based tools provide (*Mathis et al., 2018; Pereira et al., 2019*). We have also demonstrated the possibility that our toolkit could be used for real-time inference, which allows for closed-loop experiments where sensory stimuli or optogenetic stimulation are controlled in response to behavioral measurements (e.g. *Bath et al. 2014; Stowers et al. 2017*). Using real-time measurements in conjunction with optogenetics or thermogenetics may be key to disentangling the causal structure of motor output from the brain—especially given that recent work has shown an animal's response to optogenetic stimulation can differ depending on the behavior it is currently performing (*Cande et al., 2018*). Real-time behavioral quantification is also particularly important as closed-loop virtual reality is quickly becoming an indispensable tool for studying sensorimotor relationships in individuals and collectives (*Stowers et al., 2017*).

Quantifying individual movement is essential for revealing the genetic (*Kain et al., 2012; Ayroles et al., 2015*) and environmental (*Bierbach et al., 2017; Akhund-Zade et al., 2019*) underpinnings of phenotypic variation in behavior—as well as the phylogeny of behavior (e.g. *Berman et al. 2014b*). Measuring individual behavioral phenotypes requires tools that are robust, scaleable, and easy-to-use, and our approach offers the ability to quickly and accurately quantify the behavior of many individuals in great detail. When combined with tools for genetic manipulations (*Ran et al., 2013; Doudna and Charpentier, 2014*), high-throughput behavioral experiments (*Alisch et al., 2018; Werkhoven et al., 2019*), and behavioral analysis (e.g. *Berman et al. 2014a; Wiltchko et al. 2015*), our methods could help to provide the data resolution and statistical power needed for dissecting the complex relationships between genes, environment, and behavioral variation.

When used together with other tools for localization and tracking (e.g. *Pérez-Escudero et al. 2014; Crall et al. 2015; Graving 2017; Romero-Ferrero et al. 2019; Wild et al. 2018; Boenisch et al. 2018*), our methods are capable of reliably measuring posture for multiple interacting individuals. The importance of measuring detailed representations of individual behavior when studying animal collectives has been well established (*Strandburg-Peshkin et al., 2013; Rosenthal et al., 2015; Strandburg-Peshkin et al., 2015, 2017*). Estimating body posture is an essential first step for unraveling the sensory networks that drive group coordination, such as vision-based networks measured via raycasting (*Strandburg-Peshkin et al., 2013; Rosenthal et al., 2015*). Additionally, using body pose estimation in combination with computational models of behavior (e.g. *Costa et al. 2019, Wiltchko et al. 2015*) and unsupervised behavioral classification methods (e.g. *Berman et al. 2014a, Pereira et al. 2019*) may allow for further dissection of how information flows through groups by revealing the networks of behavioral contagion across multiple timescales and sensory modalities.

When combined with unmanned aerial vehicles (UAVs; *Schiffman 2014*) or other field-based imaging (*Francisco et al., 2019*), applying these methods to the study of individuals and groups in the wild can provide high-resolution behavioral data that goes beyond the capabilities of current GPS and accelerometry-based technologies (*Nagy et al., 2010, 2013; Kays et al., 2015; Strandburg-Peshkin et al., 2015, 2017; Flack et al., 2018*)—especially for species that cannot be studied with tags or collars. Additionally, by applying these methods in conjunction with 3-D habitat reconstruction—using techniques such as photogrammetry—field-based studies can begin to integrate fine-scale behavioral measurements with the full 3-D environment in which the behavior evolved (e.g. *Strandburg-Peshkin et al. 2017; Francisco et al. 2019*). This combination of technologies could allow researchers to address questions about the behavioral ecology of animals that were previously impossible to answer.

In conclusion, we have presented a toolkit, called DeepPoseKit, for automatically measuring animal posture from images. Our methods are fast, robust, and widely applicable to a range of species and experimental conditions. When designing our framework we emphasized usability across our entire software interface, which we expect will help to make these advanced tools acces-

sible to a wider range of researchers. The fast inference and real-time capabilities of our methods should also help further reduce barriers to previously intractable questions across many scientific disciplines—including neuroscience, ethology, and behavioral ecology—both in the laboratory and the field.

## Author contributions

J.M.G and I.D.C conceived the idea for the project. J.M.G. and D.C. developed the software with input from H.N. J.M.G implemented the pose estimation models and developed the subpixel maxima algorithm. J.M.G. and D.C. developed the annotation GUI, data augmentation pipeline, and wrote the documentation. J.M.G., D.C. and H.N. designed the experiments. J.M.G. and D.C. ran the experiments. B.R.C., B.K., J.M.G., and I.D.C. conceived the idea to apply posture tracking to zebras. B.R.C. and B.K. provided the annotated zebra posture data. B.K., and L.L. helped with initial testing and improvement of the software interface. L.L. also made significant contributions to an earlier version of the manuscript. J.M.G. fit the linear models and made the figures. J.M.G. wrote the initial draft of the manuscript with input from H.N. and D.C., and all authors helped revise the manuscript.

## Acknowledgements

We are indebted to Talmo Pereira et al. and A. Mathis et al. for making their software open-source and freely-available—this project would not have been possible without them. We also thank M. Mathis and A. Mathis for their comments on the manuscript. We thank François Chollet, the Keras and TensorFlow teams, and Alexander Jung for their open source contributions, which provided the core programming interface for our work. We thank Vivek H. Sridhar, Michael L. Smith, and Joseph B. Bak-Coleman for their helpful discussions on the project. We also thank M.L.S. for the use of his GPU. We thank Felicitas Oehler for annotating the zebra posture data and Chiara Hirschhorn for assistance with filming the locusts and annotating the locust posture data. We thank Alex Bruttel, Christine Bauer, Jayme Weglarski, Dominique Leo, and loobio GmbH for providing technical support. We acknowledge the NVIDIA Corporation for their generous donations to our research. This project received funding from the European Union's Horizon 2020 research and innovation programme under the Marie Skłodowska-Curie grant agreement No. 748549. B.R.C. acknowledges support from the University of Konstanz Zukunftskolleg's Investment Grant program. I.D.C. acknowledges support from NSF Grant IOS-1355061, Office of Naval Research Grants N00014-09-1-1074 and N00014-14-1-0635, Army Research Office Grants W911NG-11-1-0385 and W911NF14-1-0431, the Struktur-und Innovationsfonds für die Forschung of the State of Baden-Württemberg, the DFG Centre of Excellence 2117 "Centre for the Advanced Study of Collective Behaviour" (ID: 422037984), and the Max Planck Society.

## Animal Ethics Statement

All procedures for collecting the zebra (*E. grevyi*) dataset were reviewed and approved by Ethikrat, the independent Ethics Council of the Max Planck Society. The zebra dataset was collected with the permission of Kenya's National Commission for Science, Technology and Innovation (NACOSTI/P/17/59088/15489 and NACOSTI/P/18/59088/21567) using drones operated by B.R.C. with the permission of the Kenya Civil Aviation Authority (authorization numbers: KCAA/OPS/2117/4 Vol. 2 (80), KCAA/OPS/2117/4 Vol. 2 (81), KCAA/OPS/2117/5 (86) and KCAA/OPS/2117/5 (87); RPAS Operator Certificate numbers: RPA/TP/0005 AND RPA/TP/000-0009).

## References

Abadi M, Agarwal A, Barham P, Brevdo E, Chen Z, Citro C, Corrado GS, Davis A, Dean J, Devin M, Ghemawat S, Goodfellow I, Harp A, Irving G, Isard M, Jia Y, Jozefowicz R, Kaiser L, Kudlur M, Levenberg J, et al., TensorFlow: Large-Scale Machine Learning on Heterogeneous Systems; 2015. <https://www.tensorflow.org/>, software available from tensorflow.org.



512 **Akhund-Zade J**, Ho S, O'Leary C, de Bivort BL. The effect of environmental enrichment on behavioral variability  
513 depends on genotype, behavior, and type of enrichment. *bioRxiv*. 2019; p. 557181.

514 **Alisch T**, Crall JD, Kao AB, Zucker D, de Bivort BL. MAPLE (modular automated platform for large-scale experi-  
515 ments), a robot for integrated organism-handling and phenotyping. *eLife*. 2018; 7:e37166.

516 **Anderson DJ**, Perona P. Toward a science of computational ethology. *Neuron*. 2014; 84(1):18–31.

517 **Andriluka M**, Iqbal U, Insafutdinov E, Pishchulin L, Milan A, Gall J, Schiele B. PoseTrack: A benchmark for human  
518 pose estimation and tracking. In: *Proceedings of the IEEE Conference on Computer Vision and Pattern Recognition*;  
519 2018. p. 5167–5176.

520 **Andriluka M**, Pishchulin L, Gehler P, Schiele B. 2D Human Pose Estimation: New Benchmark and State of the  
521 Art Analysis. In: *IEEE Conference on Computer Vision and Pattern Recognition (CVPR)*; 2014. .

522 **Ayinde BO**, Zurada JM. Building efficient convnets using redundant feature pruning. *arXiv preprint*  
523 *arXiv:180207653*. 2018; .

524 **Ayroles JF**, Buchanan SM, O'Leary C, Skutt-Kakaria K, Grenier JK, Clark AG, Hartl DL, de Bivort BL. Behavioral  
525 idiosyncrasy reveals genetic control of phenotypic variability. *Proceedings of the National Academy of*  
526 *Sciences*. 2015; 112(21):6706–6711.

527 **Badrinarayanan V**, Kendall A, Cipolla R. SegNet: A Deep Convolutional Encoder-Decoder Architecture for Image  
528 Segmentation. *CoRR*. 2015; abs/1511.00561. <http://arxiv.org/abs/1511.00561>.

529 **Bath DE**, Stowers JR, Hörmann D, Poehlmann A, Dickson BJ, Straw AD. FlyMAD: rapid thermogenetic control of  
530 neuronal activity in freely walking *Drosophila*. *Nature methods*. 2014; 11(7):756.

531 **Berman GJ**. Measuring behavior across scales. *BMC biology*. 2018; 16(1):23.

532 **Berman GJ**, Bialek W, Shaevitz JW. Predictability and hierarchy in *Drosophila* behavior. *Proceedings of the*  
533 *National Academy of Sciences*. 2016; 113(42):11943–11948.

534 **Berman GJ**, Choi DM, Bialek W, Shaevitz JW. Mapping the stereotyped behaviour of freely moving fruit flies.  
535 *Journal of The Royal Society Interface*. 2014; 11(99):20140672.

536 **Berman GJ**, Choi DM, Bialek W, Shaevitz JW. Mapping the structure of drosophilid behavior. *bioRxiv*. 2014; p.  
537 002873.

538 **Bierbach D**, Laskowski KL, Wolf M. Behavioural individuality in clonal fish arises despite near-identical rearing  
539 conditions. *Nature communications*. 2017; 8:15361.

540 **Boenisch F**, Rosemann B, Wild B, Dormagen D, Wario F, Landgraf T. Tracking All Members of a Honey Bee  
541 Colony Over Their Lifetime Using Learned Models of Correspondence. *Frontiers in Robotics and AI*. 2018;  
542 5:35. <https://www.frontiersin.org/article/10.3389/frobt.2018.00035>, doi: 10.3389/frobt.2018.00035.

543 **Brown AE**, De Bivort B. Ethology as a physical science. *Nature Physics*. 2018; p. 1.

544 **Cande J**, Namiki S, Qiu J, Korff W, Card GM, Shaevitz JW, Stern DL, Berman GJ. Optogenetic dissection of  
545 descending behavioral control in *Drosophila*. *Elife*. 2018; 7:e34275.

546 **Cao Z**, Simon T, Wei SE, Sheikh Y. Realtime multi-person 2d pose estimation using part affinity fields. In:  
547 *Proceedings of the IEEE Conference on Computer Vision and Pattern Recognition*; 2017. p. 7291–7299.

548 **Carpenter B**, Lee D, Brubaker MA, Riddell A, Gelman A, Goodrich B, Guo J, Hoffman M, Betancourt M, Li P. Stan:  
549 A Probabilistic Programming Language. *J Stat Softw*. 2017; .

550 **Cauchy A**. Méthode générale pour la résolution des systemes d'équations simultanées. *Comp Rend Sci Paris*.  
551 1847; 25(1847):536–538.

552 **Chen Y**, Shen C, Wei XS, Liu L, Yang J. Adversarial posenet: A structure-aware convolutional network for human  
553 pose estimation. In: *Proceedings of the IEEE International Conference on Computer Vision*; 2017. p. 1212–1221.

554 **Chollet F**, et al., Keras. GitHub; 2015. <https://github.com/fchollet/keras>.

555 **Chollet F**. Xception: Deep learning with depthwise separable convolutions. In: *Proceedings of the IEEE conference*  
556 *on computer vision and pattern recognition*; 2017. p. 1251–1258.

557 **Costa AC**, Ahamed T, Stephens GJ. Adaptive, locally linear models of complex dynamics. *Proceedings of the*  
558 *National Academy of Sciences*. 2019; 116(5):1501–1510. <https://www.pnas.org/content/116/5/1501>, doi:  
559 [10.1073/pnas.1813476116](https://doi.org/10.1073/pnas.1813476116).

560 **Crall JD**, Gravish N, Mountcastle AM, Combes SA. BEETag: a low-cost, image-based tracking system for the study  
561 of animal behavior and locomotion. *PLoS one*. 2015; 10(9):e0136487.

562 **Dell AI**, Bender JA, Branson K, Couzin ID, de Polavieja GG, Noldus LP, Pérez-Escudero A, Perona P, Straw AD,  
563 Wikelski M, et al. Automated image-based tracking and its application in ecology. *Trends in ecology &*  
564 *evolution*. 2014; 29(7):417–428.

565 **Deng J**, Dong W, Socher R, Li LJ, Li K, Fei-Fei L. Imagenet: A large-scale hierarchical image database. . 2009; .

566 **Doudna JA**, Charpentier E. The new frontier of genome engineering with CRISPR-Cas9. *Science*. 2014;  
567 346(6213):1258096.

568 **Duane S**, Kennedy AD, Pendleton BJ, Roweth D. Hybrid Monte Carlo. *Phys Lett B*. 1987; 195(2):216–222.

569 **Dugas C**, Bengio Y, Bélisle F, Nadeau C, Garcia R. Incorporating second-order functional knowledge for better  
570 option pricing. In: *Advances in neural information processing systems*; 2001. p. 472–478.

571 **Flack A**, Nagy M, Fiedler W, Couzin ID, Wikelski M. From local collective behavior to global migratory patterns in  
572 white storks. *Science*. 2018; 360(6391):911–914.

573 **Francisco FA**, Nührenberg P, Jordan AL. A low-cost, open-source framework for tracking and behavioural analysis  
574 of animals in aquatic ecosystems. *bioRxiv*. 2019; <https://www.biorxiv.org/content/early/2019/03/09/571232>,  
575 doi: 10.1101/571232.

576 **Goodfellow I**, Bengio Y, Courville A. Deep learning. MIT press; 2016.

577 **Graving JM**, pinpoint: behavioral tracking using 2D barcode tags v0.0.1-alpha; 2017. [https://doi.org/10.5281/](https://doi.org/10.5281/zenodo.1008970)  
578 [zenodo.1008970](https://doi.org/10.5281/zenodo.1008970), doi: [10.5281/zenodo.1008970](https://doi.org/10.5281/zenodo.1008970).

579 **Guizar-Sicairos M**, Thurman ST, Fienup JR. Efficient subpixel image registration algorithms. *Optics letters*. 2008;  
580 33(2):156–158.

581 **He K**, Zhang X, Ren S, Sun J. Deep residual learning for image recognition. In: *Proceedings of the IEEE conference*  
582 *on computer vision and pattern recognition*; 2016. p. 770–778.

583 **Hoffman MD**, Gelman A. The No-U-Turn sampler: adaptively setting path lengths in Hamiltonian Monte Carlo.  
584 *Journal of Machine Learning Research*. 2014; 15(1):1593–1623.

585 **Huang G**, Liu Z, Van Der Maaten L, Weinberger KQ. Densely connected convolutional networks. In: *Proceedings*  
586 *of the IEEE conference on computer vision and pattern recognition*; 2017. p. 4700–4708.

587 **Huang J**, Rathod V, Sun C, Zhu M, Korattikara A, Fathi A, Fischer I, Wojna Z, Song Y, Guadarrama S, et al.  
588 Speed/accuracy trade-offs for modern convolutional object detectors. In: *Proceedings of the IEEE conference on*  
589 *computer vision and pattern recognition*; 2017. p. 7310–7311.

590 **Insafutdinov E**, Pishchulin L, Andres B, Andriluka M, Schiele B. Deepcut: A deeper, stronger, and faster  
591 multi-person pose estimation model. In: *European Conference on Computer Vision* Springer; 2016. p. 34–50.

592 **Iqbal U**, Milan A, Gall J. PoseTrack: Joint multi-person pose estimation and tracking. In: *Proceedings of the IEEE*  
593 *Conference on Computer Vision and Pattern Recognition*; 2017. p. 2011–2020.

594 **Jégou S**, Drozdal M, Vázquez D, Romero A, Bengio Y. The One Hundred Layers Tiramisu: Fully Convolutional  
595 DenseNets for Semantic Segmentation. *CoRR*. 2017; abs/1611.09326. <http://arxiv.org/abs/1611.09326>.

596 **Johnson M**, Duvenaud DK, Wiltchko A, Adams RP, Datta SR. Composing graphical models with neural networks  
597 for structured representations and fast inference. In: *Advances in neural information processing systems*; 2016.  
598 p. 2946–2954.

599 **Jolles JW**, Boogert NJ, Sridhar VH, Couzin ID, Manica A. Consistent individual differences drive collective behavior  
600 and group functioning of schooling fish. *Current Biology*. 2017; 27(18):2862–2868.

601 **Jung A**, imgaug. GitHub; 2018. <https://github.com/aleju/imgaug>.

602 **Kain J**, Stokes C, Gaudry Q, Song X, Foley J, Wilson R, De Bivort B. Leg-tracking and automated behavioural  
603 classification in *Drosophila*. *Nature communications*. 2013; 4:1910.

604 **Kain JS**, Stokes C, de Bivort BL. Phototactic personality in fruit flies and its suppression by serotonin and white.  
605 *Proceedings of the National Academy of Sciences*. 2012; 109(48):19834–19839.

606 **Kays R**, Crofoot MC, Jetz W, Wikelski M. Terrestrial animal tracking as an eye on life and planet. *Science*. 2015;  
607 348(6240):aaa2478.

608 **Ke L**, Chang MC, Qi H, Lyu S. Multi-Scale Structure-Aware Network for Human Pose Estimation. In: *The European*  
609 *Conference on Computer Vision (ECCV)*; 2018. .

610 **Kendall A**, Gal Y. What uncertainties do we need in bayesian deep learning for computer vision? In: *Advances in*  
611 *neural information processing systems*; 2017. p. 5574–5584.

612 **Kiefer J**, Wolfowitz J, et al. Stochastic estimation of the maximum of a regression function. *The Annals of*  
613 *Mathematical Statistics*. 1952; 23(3):462–466.

614 **Kingma DP**, Ba J. Adam: A method for stochastic optimization. *arXiv preprint arXiv:1412.6980*. 2014; .

615 **Klambauer G**, Unterthiner T, Mayr A, Hochreiter S. Self-normalizing neural networks. In: *Advances in neural*  
616 *information processing systems*; 2017. p. 971–980.

617 **Klibaite U**, Berman GJ, Cande J, Stern DL, Shaevitz JW. An unsupervised method for quantifying the behavior of  
618 paired animals. *Physical biology*. 2017; 14(1):015006.

619 **Klibaite U**, Shaevitz JW. Interacting fruit flies synchronize behavior. *bioRxiv*. 2019; p. 545483.

620 **Krakauer JW**, Ghazanfar AA, Gomez-Marin A, MacIver MA, Poeppel D. Neuroscience needs behavior: correcting  
621 a reductionist bias. *Neuron*. 2017; 93(3):480–490.

622 **Kuhn M**, Johnson K. *Applied predictive modeling*, vol. 26. Springer; 2013.

623 **LeCun Y**, Bengio Y, Hinton G. Deep learning. *nature*. 2015; 521(7553):436.

624 **Li H**, Xu Z, Taylor G, Studer C, Goldstein T. Visualizing the loss landscape of neural nets. In: *Advances in Neural*  
625 *Information Processing Systems*; 2018. p. 6391–6401.

626 **Long J**, Shelhamer E, Darrell T. Fully convolutional networks for semantic segmentation. In: *Proceedings of the*  
627 *IEEE conference on computer vision and pattern recognition*; 2015. p. 3431–3440.

628 **Markowitz JE**, Gillis WF, Beron CC, Neufeld SQ, Robertson K, Bhagat ND, Peterson RE, Peterson E, Hyun M,  
629 Linderman SW, et al. The striatum organizes 3D behavior via moment-to-moment action selection. *Cell*. 2018;  
630 174(1):44–58.

631 **Mathis A**, Mamidanna P, Cury KM, Abe T, Murthy VN, Mathis MW, Bethge M. DeepLabCut: markerless pose  
632 estimation of user-defined body parts with deep learning. *Nature Neuroscience*. 2018; <https://www.nature.com/articles/s41593-018-0209-y>.

634 **Mathis A**, Warren RA. On the inference speed and video-compression robustness of DeepLabCut. *bioRxiv*.  
635 2018; <https://www.biorxiv.org/content/early/2018/10/30/457242>, doi: 10.1101/457242.

636 **Mendes CS**, Bartos I, Akay T, Márka S, Mann RS. Quantification of gait parameters in freely walking wild type  
637 and sensory deprived *Drosophila melanogaster*. *elife*. 2013; 2:e00231.

638 **Nagy M**, Akos Z, Biro D, Vicsek T. Hierarchical group dynamics in pigeon flocks. *Nature*. 2010; 464(7290):890.

639 **Nagy M**, Vásárhelyi G, Pettit B, Roberts-Mariani I, Vicsek T, Biro D. Context-dependent hierarchies in pigeons.  
640 *Proceedings of the National Academy of Sciences*. 2013; 110(32):13049–13054.

641 **Nath T**, Mathis A, Chen AC, Patel A, Bethge M, Mathis MW. Using DeepLabCut for 3D markerless pose estimation  
642 across species and behaviors. *bioRxiv*. 2018; <https://www.biorxiv.org/content/early/2018/11/24/476531>, doi:  
643 10.1101/476531.

644 **Newell A**, Yang K, Deng J. Stacked Hourglass Networks for Human Pose Estimation. *CoRR*. 2016; abs/1603.06937.  
645 <http://arxiv.org/abs/1603.06937>.

646 **Pereira TD**, Aldarondo DE, Willmore L, Kislin M, Wang SSH, Murthy M, Shaevitz JW. Fast animal pose estimation  
647 using deep neural networks. *Nature methods*. 2019; 16(1):117.

648 **Pérez-Escudero A**, Vicente-Page J, Hinz RC, Arganda S, De Polavieja GG. idTracker: tracking individuals in a  
649 group by automatic identification of unmarked animals. *Nature methods*. 2014; 11(7):743.

650 **Pratt LY**. Discriminability-based transfer between neural networks. In: *Advances in neural information processing*  
651 *systems*; 1993. p. 204–211.

652 **Prechelt L**. Automatic early stopping using cross validation: quantifying the criteria. *Neural Networks*. 1998;  
653 11(4):761–767.

654 **Ran FA**, Hsu PD, Wright J, Agarwala V, Scott DA, Zhang F. Genome engineering using the CRISPR-Cas9 system.  
655 *Nature protocols*. 2013; 8(11):2281.

656 **Robbins H**, Monro S. A stochastic approximation method. *The annals of mathematical statistics*. 1951; p.  
657 400–407.

658 **Romero-Ferrero F**, Bergomi MG, Hinz RC, Heras FJ, de Polavieja GG. idtracker. ai: tracking all individuals in  
659 small or large collectives of unmarked animals. *Nature methods*. 2019; 16(2):179.

660 **Ronneberger O**, Fischer P, Brox T. U-net: Convolutional networks for biomedical image segmentation. In:  
661 *International Conference on Medical image computing and computer-assisted intervention* Springer; 2015. p.  
662 234–241.

663 **Rosenthal SB**, Twomey CR, Hartnett AT, Wu HS, Couzin ID. Revealing the hidden networks of interaction in  
664 mobile animal groups allows prediction of complex behavioral contagion. *Proceedings of the National*  
665 *Academy of Sciences*. 2015; 112(15):4690–4695.

666 **Roy AG**, Conjeti S, Navab N, Wachinger C. Bayesian QuickNAT: Model Uncertainty in Deep Whole-Brain Segmen-  
667 tation for Structure-wise Quality Control. *CoRR*. 2018; abs/1811.09800. <http://arxiv.org/abs/1811.09800>.

668 **Sabour S**, Frosst N, Hinton GE. Dynamic routing between capsules. In: *Advances in neural information processing*  
669 *systems*; 2017. p. 3856–3866.

670 **Sandler M**, Howard A, Zhu M, Zhmoginov A, Chen LC. Mobilenetv2: Inverted residuals and linear bottlenecks.  
671 In: *Proceedings of the IEEE Conference on Computer Vision and Pattern Recognition*; 2018. p. 4510–4520.

672 **Schiffman R**, Drones flying high as new tool for field biologists. *American Association for the Advancement of*  
673 *Science*; 2014.

674 **Stowers JR**, Hofbauer M, Bastien R, Griessner J, Higgins P, Farooqui S, Fischer RM, Nowikovsky K, Haubensak W,  
675 Couzin ID, et al. Virtual reality for freely moving animals. *Nature methods*. 2017; 14(10):995.

676 **Strandburg-Peshkin A**, Farine DR, Couzin ID, Crofoot MC. Shared decision-making drives collective movement  
677 in wild baboons. *Science*. 2015; 348(6241):1358–1361.

678 **Strandburg-Peshkin A**, Farine DR, Crofoot MC, Couzin ID. Habitat and social factors shape individual decisions  
679 and emergent group structure during baboon collective movement. *Elife*. 2017; 6:e19505.

680 **Strandburg-Peshkin A**, Twomey CR, Bode NW, Kao AB, Katz Y, Ioannou CC, Rosenthal SB, Torney CJ, Wu HS,  
681 Levin SA, et al. Visual sensory networks and effective information transfer in animal groups. *Current Biology*.  
682 2013; 23(17):R709–R711.

683 **Todd JG**, Kain JS, de Bivort BL. Systematic exploration of unsupervised methods for mapping behavior. *Physical*  
684 *biology*. 2017; 14(1):015002.

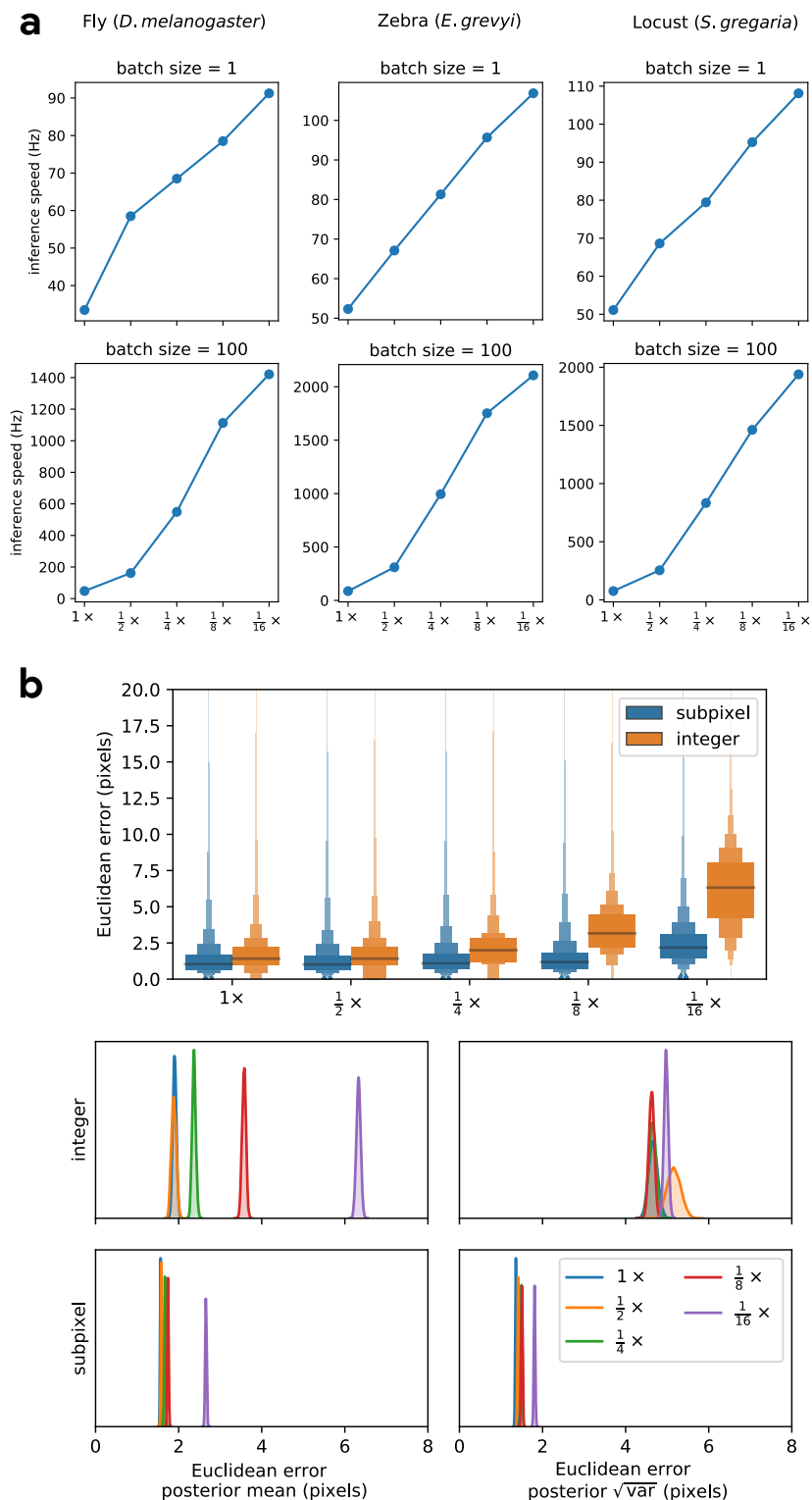
685 **Tran D**, Hoffman MW, Moore D, Suter C, Vasudevan S, Radul A. Simple, distributed, and accelerated probabilistic  
686 programming. In: *Advances in Neural Information Processing Systems*; 2018. p. 7609–7620.

687 **Uhlmann V**, Ramdya P, Delgado-Gonzalo R, Benton R, Unser M. FlyLimbTracker: An active contour based  
688 approach for leg segment tracking in unmarked, freely behaving *Drosophila*. *PLoS One*. 2017; 12(4):e0173433.

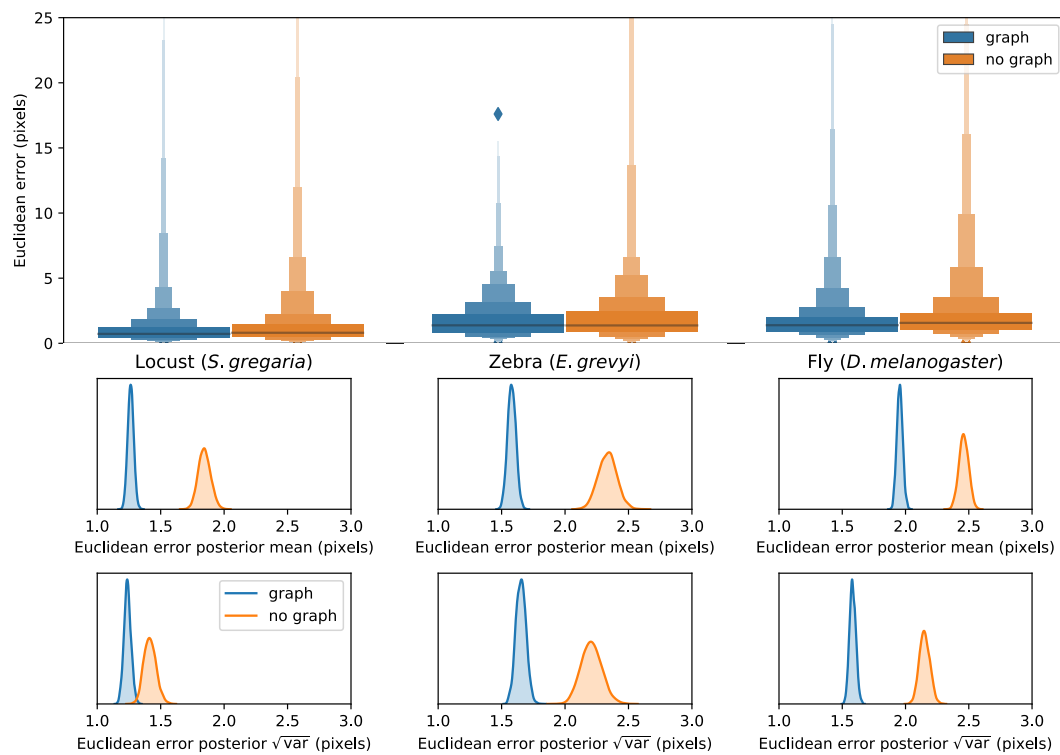
689 **Weigert M**, Schmidt U, Boothe T, Müller A, Dibrov A, Jain A, Wilhelm B, Schmidt D, Broaddus C, Culley S, et al.  
690 Content-aware image restoration: pushing the limits of fluorescence microscopy. *Nature methods*. 2018;  
691 15(12):1090.

- 692 **Werkhoven Z**, Rohrsen C, Qin C, Brembs B, de Bivort B. MARGO (Massively Automated Real-time GUI for  
693 Object-tracking), a platform for high-throughput ethology. *BioRxiv*. 2019; p. 593046.
- 694 **Wild B**, Sixt L, Landgraf T. Automatic localization and decoding of honeybee markers using deep convolutional  
695 neural networks. *CoRR*. 2018; abs/1802.04557. <http://arxiv.org/abs/1802.04557>.
- 696 **Wiltchko AB**, Johnson MJ, Iurilli G, Peterson RE, Katon JM, Pashkovski SL, Abaira VE, Adams RP, Datta SR.  
697 Mapping sub-second structure in mouse behavior. *Neuron*. 2015; 88(6):1121–1135.

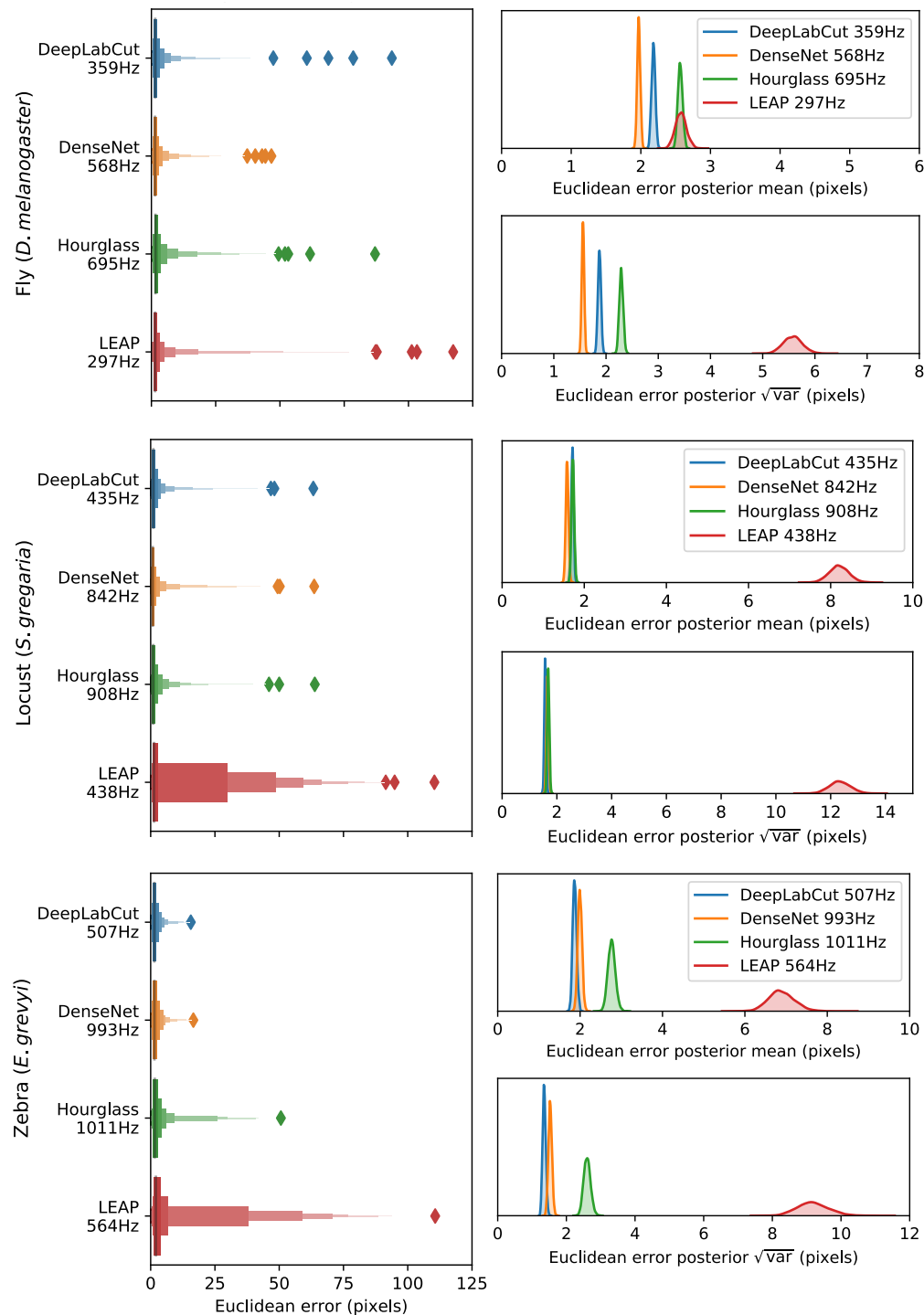




**Appendix 0 Figure 5.** Our subpixel maxima algorithm increases speed (**a**) without decreasing accuracy (**b**). Inference speed is fast and can be run in real-time on single images (batch size = 1) at ~30-110Hz. Plots show the inference speeds for our Stacked DenseNet model across downsampling configurations for each of our datasets (**a**). Prediction accuracy on the fly dataset is maintained across downsampling configurations (**b**). Letter-value plots (**top**) show the raw error distributions for each configuration. Visualizations of the posterior distributions for the mean and variance (**bottom**) illustrate statistical differences between the error distributions, where using subpixel maxima decreases both the mean and variance of the error distribution.



**Appendix 0 Figure 6.** Predicting the global geometry of the posture graph reduces error. Letter-value plots (**top**) show the raw error distributions for each experiment. Visualizations of the posterior distributions for the mean and variance (**bottom**) show statistical differences between the error distributions. Predicting the posture graph decreases both the mean and variance of the error distribution.



**Appendix 0 Figure 7.** Euclidean error distributions for each model across our three datasets. Letter-value plots (**left**) show the raw error distributions for each model. Histograms of the posterior distributions for the mean and variance (**right**) show statistical differences between the error distributions. Overall the LEAP model from *Pereira et al. (2019)* was the worst performer on every dataset in terms of both mean and variance. Our implementation of Stacked Densenet was the best performer for the fly dataset, while Stacked DenseNet and DeepLabCut both performed equally well on the locust and zebra datasets. The posteriors for DeepLabCut (*Mathis et al., 2018*) and our Stacked DenseNet model are highly overlapping for these datasets, which suggests they are not statistically discernible from one another. The Stacked Hourglass (*Newell et al., 2016*) model performed slightly worse than DeepLabCut and our Stacked DenseNet model for all datasets.

## 698 Appendix 1

### 699 Convolutional neural networks (CNNs)

700 *Artificial neural networks* like CNNs are complex, non-linear regression models that "learn"  
701 a hierarchically-organized set of parameters from real-world data via optimization. These  
702 machine learning models are now commonplace in science and industry and have proven  
703 to be surprisingly effective for a large number of applications where more conventional  
704 statistical models have failed (**LeCun et al., 2015**). For computer vision tasks, CNN parameters  
705 typically take the form of two-dimensional convolutional filters that are optimized to detect  
706 spatial features needed to model relationships between high-dimensional image data and  
707 some related variable(s) of interest, such as locations in space—e.g. posture keypoints—or  
708 semantic labels (**Long et al., 2015; Badrinarayanan et al., 2015**).

709 Once a training set is generated (Appendix 2), a CNN model must be selected and  
710 optimized to perform the prediction task. CNNs are incredibly flexible with regard to how  
711 models are specified and trained, which is both an advantage and a disadvantage. This  
712 flexibility means models can be adapted to almost any computer vision task, but it also  
713 means the number of possible model architectures and optimization schemes is very large.  
714 This can make selecting an architecture and specifying hyperparameters a challenging  
715 process. However, most research on pose estimation has converged on a set of models that  
716 generally work well for this task (Appendix 3).

717 After selecting an architecture, the parameters of the model are set to an initial value and  
718 then iteratively updated to minimize some objective function, or *loss function*, that describes  
719 the difference between the model's predictive distribution and the true distribution of the  
720 data—in other words, the likelihood of the model's output is maximized. These parameter  
721 updates are performed using a modified version of the gradient descent algorithm (**Cauchy**  
722 **1847**) known as *mini-batch stochastic gradient descent*—often referred to as simply *stochastic*  
723 *gradient descent* or *SGD* (**Robbins and Monro, 1951; Kiefer et al., 1952**). SGD iteratively  
724 optimizes the model parameters using small randomly-selected subsamples, or *batches*,  
725 of training data. Using SGD allows the model to be trained on extremely large datasets  
726 in an iterative "online" fashion without the need to load the entire dataset into memory.  
727 The model parameters are updated with each batch by adjusting the parameter values in  
728 a direction that minimizes the error—where one round of training on the full dataset is  
729 commonly referred to as an *epoch*. The original SGD algorithm requires careful selection and  
730 tuning of hyperparameters to successfully optimize a model, but modern versions of the  
731 algorithm, such as *ADAM* (**Kingma and Ba, 2014**), automatically tune these hyperparameters,  
732 which makes optimization more straightforward.

733 The model parameters are optimized until they reach a convergence criterion, which  
734 is some measure of performance that indicates the model has reached a good location in  
735 parameter space. The most commonly used convergence criterion is a measure of predictive  
736 accuracy—often the loss function used for optimization—on a held-out *validation set*—a  
737 subsample of the training data not used for optimization—that evaluates the model's ability  
738 to generalize to new "out-of-sample" data. The model is typically evaluated at the end of  
739 each training epoch to assess performance on the validation set. Once performance on  
740 the validation set stops improving, training is usually stopped to prevent the model from  
741 overfitting to the training set—a technique known as *early stopping* (**Prechelt, 1998**).

## 742 Appendix 2

### 743 Collecting training data

744 Depending on the variability of the data, CNNs usually require thousands or tens of thou-  
745 sands of manually-annotated examples in order to reach human-level accuracy. However, in  
746 laboratory settings, sources of image variation like lighting and spatial scale can be more  
747 easily controlled, which minimizes the number of training examples needed to achieve  
748 accurate predictions.

749 This need for a large training set can be further reduced in a number of ways. Two  
750 commonly used methods include (1) *transfer learning*—using a model with parameters that  
751 are pre-trained on a larger set of images, such as the ImageNet database (*Deng et al., 2009*),  
752 containing diverse features (*Pratt, 1993; Insafutdinov et al., 2016; Mathis et al., 2018*)—  
753 and (2) *augmentation*—artificially increasing data variance by applying spatial and noise  
754 transformations such as flipping (mirroring), rotating, scaling, and adding different forms  
755 of noise or artificial occlusions. Both of these methods act as useful forms of *regulariza-*  
756 *tion*—incorporating a prior distribution—that allows the model to generalize well to new  
757 data even when the training set is small. Transfer learning incorporates prior information  
758 that images from the full dataset should contain statistical features similar to other images  
759 of the natural world, while augmentation incorporates prior knowledge that animals are  
760 bilaterally symmetric, can vary in their body size, position, and orientation, and that noise  
761 and occlusions sometimes occur.

762 *Pereira et al. (2019)* introduced two especially clever solutions for collecting an adequate  
763 training set. First, they cluster unannotated images based on pixel variance and uniformly  
764 sample images from each cluster, which reduces correlation between training examples  
765 and ensures the training data are representative of the entire distribution of possible  
766 images. Second, they use *active learning* where a CNN is trained on a small number of  
767 annotated examples and is then used to initialize keypoint locations for a larger set of  
768 unannotated data. These pre-initialized data are then manually corrected by the annotator,  
769 the model is retrained, and the unannotated data are re-initialized. The annotator applies  
770 this process iteratively as the training set grows larger until they are providing only minor  
771 adjustments to the pre-initialized data. This “human-in-the-loop”-style annotation expedites  
772 the process of generating an adequately large training set by reducing the cognitive load  
773 on the annotator—where the pose estimation model serves as a “cognitive partner”. Such  
774 a strategy also allows the annotator to automatically select new training examples based  
775 on the performance of the current iteration—where low-confidence predictions indicate  
776 examples that should be annotated for maximum improvement (Figure 1).

777 Of course, annotating image data requires software made for this purpose. *Pereira*  
778 *et al. (2019)* provide a custom annotation GUI written in MATLAB specifically designed for  
779 annotating posture using an active learning strategy. *Mathis et al. (2018)* originally did  
780 not provide a custom annotation tool with active learning, but recently added a Python-  
781 based GUI in an updated version of their software—including active learning and image  
782 sampling methods (see *Nath et al. 2018*). Our framework also includes a Python-based GUI  
783 for annotating data with similar features to *Mathis et al. (2018)* and *Pereira et al. (2019)*.

## 784 Appendix 3

### 785 Fully-convolutional regression

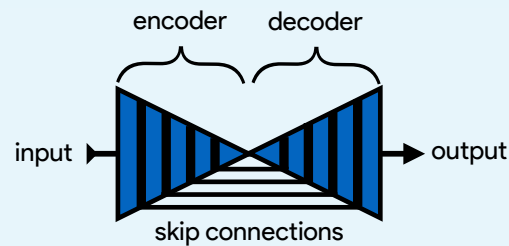
786 For the task of pose estimation, a CNN is optimized to predict the locations of postural  
787 keypoints in an image. One approach is to use a CNN to directly predict the numerical  
788 value of each keypoint coordinate as an output. However, making predictions in this way  
789 removes real-world constraints on the model's predictive distribution by destroying spatial  
790 relationships within images, which negates many of the advantages of using CNNs in the  
791 first place.

792 CNNs are particularly good at transforming one image to produce another related  
793 image, or set of images, while preserving spatial relationships and allowing for translation-  
794 invariant predictions—a configuration known as a *fully-convolutional neural network* or *F-  
795 CNN* (Long et al., 2015). Therefore, instead of directly regressing images to coordinate  
796 values, a popular solution (Newell et al., 2016; Insafutdinov et al., 2016; Mathis et al., 2018;  
797 Pereira et al., 2019) is to optimize a F-CNN that transforms images to predict a stack of  
798 output images known as *confidence maps*—one for each keypoint. Each confidence map in  
799 the output volume contains a single, two-dimensional, symmetric Gaussian indicating the  
800 location of each joint, and the scalar value of the peak indicates the confidence score of the  
801 prediction—typically a value between 0 and 1. The confidence maps are then processed to  
802 produce the coordinates of each keypoint.

803 In the case of *multiple pose estimation* where an image contains many individuals, the  
804 global geometry of the posture graph is also predicted by training the model to produce *part  
805 affinity fields* (Cao et al., 2017)—vector fields drawn between joints in the posture graph—or  
806 *pairwise terms* (Insafutdinov et al., 2016)—vector fields of the conditional distributions  
807 between posture keypoints (e.g.  $p(\text{foot}|\text{head})$ ). This allows multiple posture graphs to be  
808 disentangled from the image using graph partitioning as the vector fields indicate the  
809 probability of the connection between joints (see Cao et al. 2017 for details).



## Box 1. Encoder-decoder models

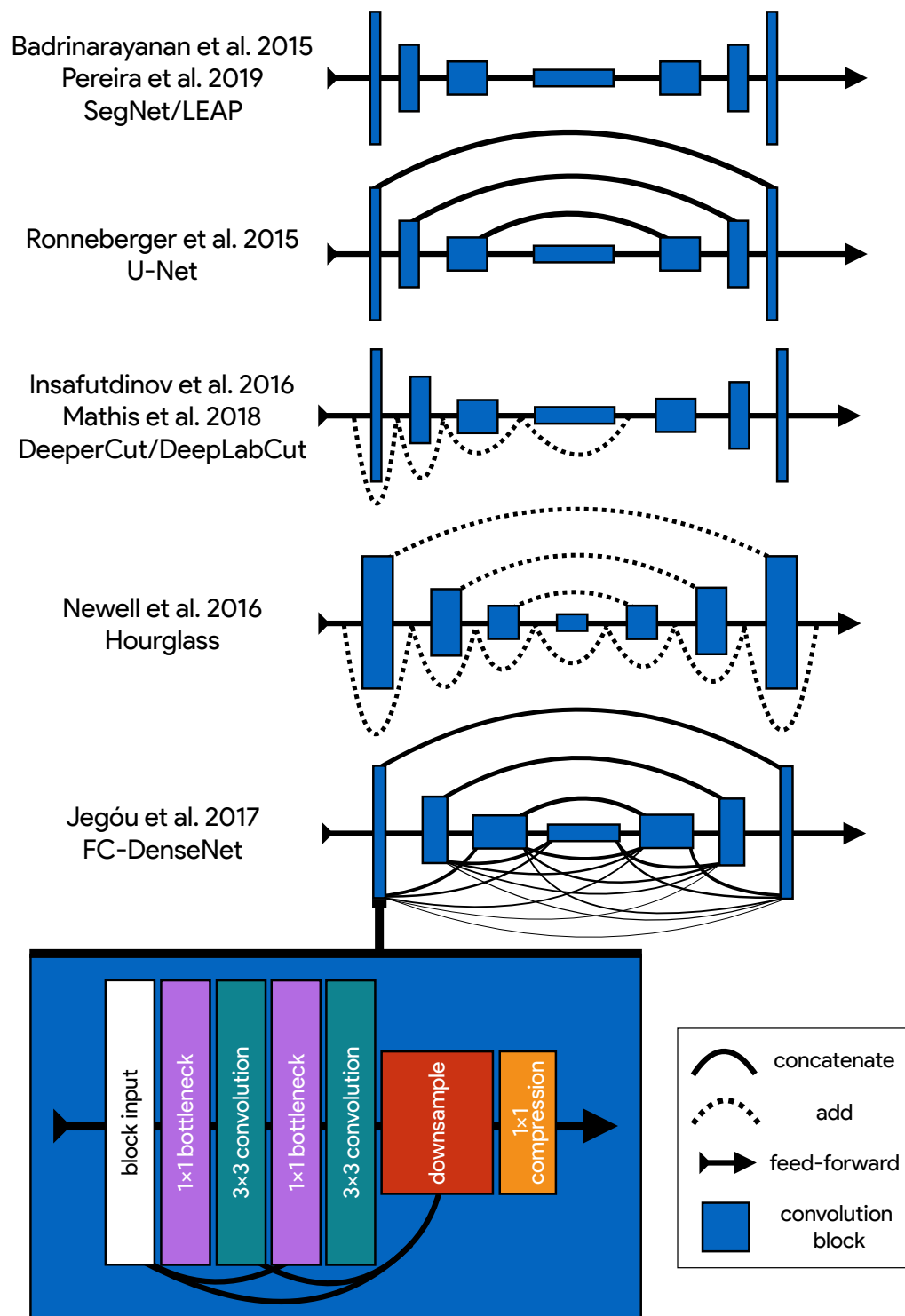


**Box 1 Figure 1.** An illustration of the basic encoder-decoder design. The encoder converts the input images into spatial features, and the decoder transforms spatial features to the desired output.

A popular type of F-CNN (Appendix 3) for solving posture regression problems is known as an *encoder-decoder* model (Figure 1), which first gained popularity for the task of semantic segmentation—a supervised computer vision problem where each pixel in an image is classified into a one of several labeled categories like “dog”, “tree”, or “road” (Long et al., 2015). This model is designed to repeatedly convolve and downsample input images in the bottom-up *encoder* step and then convolve and upsample the encoder’s output in the top-down *decoder* step to produce the final output. Repeatedly applying convolutions and non-linear functions, or *activations*, to the input images transforms pixel values into higher-order spatial features, while downsampling and upsampling respectively increases and decreases the scale and complexity of these features.

Badrinarayanan et al. (2015) were the first to popularize a form of this model—known as *SegNet*—for semantic segmentation. However, this basic design is inherently limited because the decoder relies solely on the downsampled output from the encoder, which restricts the features used for predictions to those with the largest spatial scale and highest complexity. For example, a very deep network might learn a complex spatial pattern for predicting “grass” or “trees”, but because it cannot directly access information from the earliest layers of the network, it cannot use the simplest features that plants are green and brown. Subsequent work by Ronneberger et al. (2015) improved on these problems with the addition of *residual* or *skip connections* between the encoder and decoder, where feature maps from encoder layers are concatenated to those decoder layers with the same spatial scale. This set of connections then allows the optimizer, rather than the user, to select the most relevant spatial scale(s) for making predictions.

Jégou et al. (2017) are the latest to advance the encoder-decoder paradigm. These researchers introduced a fully-convolutional version of Huang et al.’s (2017a) *DenseNet* architecture known as a *fully-convolutional DenseNet*, or *FC-DenseNet*. FC-DenseNet’s key improvement is an elaborate set of feed-forward residual connections where the input to each convolutional layer is a concatenated stack of feature maps from *all previous layers*. This densely-connected design was motivated by the insight that many state-of-the-art models learn a large proportion of redundant features. Most CNNs are not designed so that the final output layers can access all feature maps in the network simultaneously, and this limitation causes these networks to “forget” and “relearn” important features as the input images are transformed to produce the output. In the case of the incredibly popular ResNet-101 (He et al., 2016) nearly 40% of the features can be classified as redundant (Ayinde and Zurada, 2018). A densely-connected architecture has the advantages of reduced feature redundancy, increased feature reuse, enhanced feature propagation from early layers to later layers, and subsequently, a *substantial reduction* in the number of parameters needed to achieve state-of-the-art results (Huang et al., 2017a). Recent work has also shown that DenseNet’s elaborate residual connections have the pleasant side-effect of convexifying the loss landscape during optimization (Li et al., 2018), which allows for faster optimization and increases the likelihood of reaching a good optimum.



**Appendix 3 Figure 1.** An illustration showing the progression of encoder-decoder architectures from the literature—ordered by performance from top to bottom (see Appendix 3 Box 1 for further details). Most advances in performance have come from adding connections between layers in the network, culminating in FC-DenseNet from *Jégou et al. (2017)*. Lines in each illustration indicate connections between convolutional blocks with the thickness of the line indicating the magnitude of information flow between layers in the network. The size of each convolution block indicates the relative number of feature maps (width) and spatial scale (height). The callout for FC-DenseNet (*Jégou et al. 2017*; **bottom-left**) shows the elaborate set of skip connections within each densely-connected convolutional block as well as our additions of bottleneck and compression layers (described by *Huang et al. 2017a*) to increase efficiency (Appendix 8)

## 854 Appendix 4

### 855 Individual vs. multiple pose estimation

856 Most recent state-of-the-art methods for posture estimation now focus on simultaneously  
857 estimating the pose of multiple individuals in an image (e.g. **Cao et al. 2017**)—known as  
858 *multiple pose estimation*. However, the majority of work on multiple pose estimation has  
859 not adequately solved the tracking problem of linking individual data across frames in a  
860 video, especially after visual occlusions—although recent work has attempted to address this  
861 problem (**Iqbal et al., 2017; Andriluka et al., 2018**). Reliably tracking individuals is important  
862 for most behavioral studies, and there are a number of diverse methods already available for  
863 solving this problem (**Pérez-Escudero et al., 2014; Crall et al., 2015; Graving, 2017; Romero-**  
864 **Ferrero et al., 2019; Wild et al., 2018; Boenisch et al., 2018**). Therefore, to avoid solving  
865 an already-solved problem, the work we describe in this paper is purposefully limited to  
866 *individual pose estimation* where each image contains only a single focal individual—which  
867 may be localized and cropped from a larger multi-individual image.

868 We created a top-down posture estimation framework that can be easily adapted to  
869 any data collection workflow, which could include any method for localizing and tracking  
870 individuals. Limiting our methods in this way also simplifies the pose detection problem  
871 and the cognitive task of creating annotated data. Additionally, because individual pose  
872 estimation is such a well-studied problem in computer vision, we can build on the state-of-  
873 the-art for this task (see Appendices 3 and 5 for details).

## 874 Appendix 5

### 875 The state of the art for individual pose estimation

876 Many of the current state-of-the-art models for individual posture estimation are based on  
 877 the design from **Newell et al. (2016)** (e.g. **Ke et al. 2018**, **Chen et al. 2017**; also see bench-  
 878 mark results from **Andriluka et al. 2014**), but employ various modifications that increase  
 879 complexity to improve performance. **Newell et al. (2016)** employ what they call a *Stacked*  
 880 *Hourglass* network (Appendix 3 Figure 1), which consists of a series of multi-scale encoder-  
 881 decoder *hourglass* modules connected together in a feed-forward configuration (Figure 2).  
 882 The main novelties these researchers introduce include (1) stacking multiple hourglass net-  
 883 works together for repeated top-down-bottom-up inference, (2) using convolutional blocks  
 884 based on the ResNet architecture (**He et al., 2016**) with residual connections between the  
 885 input and output of each block, and (3) using residual connections between the encoder  
 886 and decoder (similar to **Ronneberger et al. 2015**) with residual blocks in between. **Newell**  
 887 **et al. (2016)** also apply a technique known as *intermediate supervision* (Figure 2) where the  
 888 loss function used for model training is applied to the output of each hourglass as a way of  
 889 improving optimization across the model's many layers. Recent work by **Jégou et al. (2017)**  
 890 has further improved on this encoder-decoder design (see Appendix 3 Box 1 and Appendix  
 891 3 Figure 1), but to the best of our knowledge, the model introduced by **Jégou et al. (2017)**  
 892 has not been previously applied to pose estimation.

## 893 Appendix 6

### 894 Overparameterization and the limitations of LEAP

895 Overparameterization is a key limitation for many pose estimation methods, and addressing  
 896 this problem is critical for high-performance applications. *Pereira et al. (2019)* approached  
 897 this problem by designing their LEAP model after the model from *Badrinarayanan et al.*  
 898 *(2015)*, which is a straightforward encoder-decoder design (Appendix 3 Figure 1; Appendix 3  
 899 Box 1). They benchmarked their model on posture estimation tasks for laboratory animals  
 900 and compared performance with the more-complex Stacked Hourglass model from *Newell*  
 901 *et al. (2016)*. They found their smaller, simplified model achieved equal or better median ac-  
 902 curacy with dramatic improvements in inference speed up to 185 Hz. However, *Pereira et al.*  
 903 *(2019)* first rotationally and translationally aligned each image to improve performance, and  
 904 their reported inference speeds do not include this computationally expensive preprocessing  
 905 step. Additionally, rotationally and translationally aligning images is not always possible  
 906 when the background is complex or highly-variable—such as in field settings—or the study  
 907 animal has a non-rigid body. This limitation makes LEAP (*Pereira et al., 2019*) unsuitable in  
 908 many cases. While their approach is simple and effective for a multitude of experimental  
 909 setups, the LEAP model from *Pereira et al. (2019)* is also implicitly limited in the same ways  
 910 as *Badrinarayanan et al.*'s SegNet model (see Appendix 3 Box 1 for details). LEAP cannot  
 911 make predictions using multiple spatial scales and is not robust to data variance such as  
 912 rotations (*Pereira et al., 2019*).

## 913 Appendix 7

### 914 Fitting linear models with Stan

915 We estimated the joint posterior  $p(\theta_\mu, \theta_\phi | X, y)$  for each model using the No-U-Turn Sampler  
 916 (NUTS; *Hoffman and Gelman 2014*), a self-tuning variant of the Hamiltonian Monte Carlo  
 917 (HMC) algorithm (*Duane et al., 1987*), implemented in Stan (*Carpenter et al., 2017*). We drew  
 918 HMC samples using 4 independent Markov chains consisting of 1,000 warm-up iterations  
 919 and 1,000 sampling iterations for a total of 4,000 sampling iterations. To speed up sampling,  
 920 we randomly subsampled 20% of the data from each replicate when fitting each linear model,  
 921 and we fit each model 5 times to ensure the results were consistent. All models converged  
 922 without any signs of pathological behavior. We performed a posterior predictive check by  
 923 visually inspecting predictive samples to assess model fit. For our priors we chose relatively  
 924 uninformative distributions  $\theta_\mu \sim \text{Cauchy}(0, 5)$  and  $\theta_\phi \sim \text{Cauchy}(0, 10)$ , but we found that the  
 925 choice of prior generally did not have an effect on the final result due to the large amount of  
 926 data used to fit each model.



## 927 Appendix 8

### 928 Stacked DenseNet

929 Our Stacked DenseNet model consists of an initial 7×7 convolutional layer with stride 2,  
930 to efficiently downsample the input resolution—following *Newell et al. (2016)*—followed  
931 by a stack of densely-connected hourglasses with intermediate supervision (Appendix 5)  
932 applied at the output of each hourglass. We also include hyperparameters for the bottleneck  
933 and compression layers described by *Huang et al. (2017a)* to make the model as efficient  
934 as possible. These consist of applying a 1×1 convolution to inexpensively compress the  
935 number of feature maps before each 3×3 convolution as well as when downsampling and  
936 upsampling (see *Huang et al. 2017a* and Appendix 3 Figure 1 for details).

### 937 Model hyperparameters

938 For our Stacked Hourglass model we used a block size of 64 filters (64 filters per 3×3  
939 convolution) with a bottleneck factor of 2 ( $64/2 = 32$  filters per 1×1 bottleneck block). For  
940 our Stacked DenseNet model we used a growth rate of 48 (48 filters per 3×3 convolution), a  
941 bottleneck factor of 1 ( $1 \times \text{growth rate} = 48$  filters per 1×1 bottleneck block), and a compression  
942 factor of 0.5 (feature maps compressed with 1×1 convolution to  $0.5m$  when upsampling  
943 and downsampling, where  $m$  is the number of feature maps). For our Stacked DenseNet  
944 model we also replaced the typical configuration of batch normalization and ReLU activations  
945 (*Goodfellow et al., 2016*) with the more recently developed self-normalizing SELU activation  
946 function (*Klambauer et al., 2017*), as we found this modification increased inference speed.  
947 For LEAP (*Pereira et al., 2019*) we used a 1× resolution output with integer-based global  
948 maxima because we wanted to compare our more complex models with LEAP in the original  
949 configuration described by *Pereira et al. (2019)*. Additionally, applying our subpixel maxima  
950 algorithm at high resolution reduces inference speed compared to integer-based maxima,  
951 so this would bias our speed comparisons.

### 952 Our implementation of DeepLabCut

953 Because the DeepLabCut model from *Mathis et al. (2018)* was not implemented in Keras  
954 (a requirement for our pose estimation framework), our implementation of this model  
955 does not exactly match the description in the paper. Implementing this model directly in  
956 our framework is important to ensure model training and data augmentation are identical  
957 when making comparisons. Nevertheless our version is nearly identical—except for the  
958 output—and should match the performance described by *Mathis et al. (2018)*. Rather  
959 than using the location refinement maps described by *Insafutdinov et al. (2016)* and post-  
960 processing confidence maps on the CPU, our implementation of *Mathis et al. (2018)* has  
961 an additional transposed convolutional layer to upsample the output to  $\frac{1}{4} \times$  resolution and  
962 takes advantage of our fast subpixel maxima algorithm, which should approximate the  
963 location refinement maps well. Our overall comparisons should be reasonable regardless  
964 of these constraints, as the core of our DeepLabCut model is identical to *Mathis et al.*  
965 *(2018)*. Because the training routine could be changed to further improve any underlying  
966 model—including the new models we present in this paper—this factor is not relevant when  
967 making comparisons as long as training is identical for all models. Our reported inference  
968 speeds for our datasets also match well with results from *Mathis and Warren (2018)* who  
969 evaluated the inference speed of DeepLabCut (*Mathis et al., 2018*) for multiple image sizes.

## 970 Appendix 9

### 971 Depthwise-separable convolutions for memory-limited applications

972 In an effort to maximize model efficiency, we also experimented with replacing 3x3 convo-  
 973 lutions in our model implementations with 3x3 depthwise-separable convolutions —first  
 974 introduced by *Chollet (2017)* and now commonly used in fast, efficient “mobile” CNNs (e.g.  
 975 *Sandler et al. 2018*). In theory this modification should both reduce the memory footprint  
 976 of the model and increase inference speed. However we found that, while this does dras-  
 977 tically decrease the memory footprint of our already memory-efficient models, it slightly  
 978 decreases accuracy and does not improve inference speed, so we opt for a full 3x3 con-  
 979 volution instead. We suspect that this discrepancy between theory and application is due  
 980 to inefficient implementations of depthwise-separable convolutions in many popular deep  
 981 learning frameworks, which will hopefully improve in the near future. At the moment we in-  
 982 clude this option as a hyperparameter for our Stacked DenseNet model, but we recommend  
 983 using depthwise-separable convolutions only for applications that require a small memory  
 984 footprint such as training on a lower-end GPU with limited memory or running inference on  
 985 a mobile device.